Carro, G., Muñoz, A., Savoini, B., Monge, M. & Pareja, R. (2019). Processing, microstructure and mechanical characterization of dispersion strengthened Cu-1%Y. *Fusion Engineering and Design*, vol. 138, pp. 321–331.

DOI: 10.1016/j.fusengdes.2018.11.058

Processing, microstructure and mechanical characterization of dispersion strengthened Cu-1%Y

G. Carro, A. Muñoz*, B. Savoini, M.A. Monge, and R. Pareja

Universidad Carlos III de Madrid, Departamento de Física, Avda de la Universidad 30, 28911-Leganés, Madrid, Spain

Abstract:

Dispersion strengthened Cu-1%Y (wt%) has been produced by mechanical alloying and subsequent consolidation by hot isostatic pressing (HIP). Samples of this alloy have been submitted to an equal channel angular pressing (ECAP) process and the effects on the microstructure and mechanical properties analyzed. The characteristics of the microstructure, such as the size distributions of both, the grains and Y-rich particles dispersed in the Cu matrix, have been studied by high resolution electron scanning microscopy and electron backscatter diffraction. The as-HIP alloy exhibits a quasi-bimodal distribution with an average diameter of 17 ± 14 μm. The ECAP treatment refines the average grain size to 1.3 ± 0.9 μm besides changing the size distribution of the Y-rich particles, which shifted from average size from 94 ± 9 nm to 55 ± 8 nm after ECAP.

The mechanical characteristics have been investigated by means of microhardness measurements, and stress-strain tests in the temperature range 293 – 573 K. The ECAP deformation resulted in an increase of the mechanical strength and a decrease in ductility. It is found that the Voce law can satisfactorily describe the plastic and hardening rate behavior of these alloys. The strain hardening rate plots as a function of flow stress for the samples tested at 293 ≤ T ≤ 773 K exhibited a two-stage behavior,

comprising a transient stage at low stresses followed by the characteristic linear dependence for the stage III of hardening in f.c.c. metals.

*Corresponding Author: angel.munoz@uc3m.es

Permanent address: Departamento de Física, Universidad Carlos III de Madrid, Avda de la Universidad, 30 28911-Leganés, Madrid (Spain)

Key words: Dispersion Strengthened copper, Equal Channel Angular pressing, Strain hardening rate, Voce model.

1. Introduction

Cu-based materials, due to their high thermal conductivity, are considered the primary candidates for heat sink materials in the plasma facing components (PFCs) of a near-term DEMO fusion reactor [1, 2]. As heat sinks attached to PFCs, these materials will have to assume certain structural functions under the high thermal and radiation loads foreseen for a DEMO reactor. Thus, in addition to high thermal conductivity and strength, other key design requirements for these high-heat flux (HHF) materials are thermal stability up to 1300 K, radiation resistance, as well as creep and fatigue resistance at elevated temperatures [3]. Precipitation hardened (PH) CuCrZr and dispersion strengthened (DS) Cu-Al_2O_3 (GlidCop) are presently considered the baseline materials for high heat flux applications in the water-cooled PFCs designs for the near-term DEMO, as there exists an important database predicting their performances under the ITER operation conditions [4, 5]. However, these HHF materials have critical limits in their working temperatures that would lower the overall efficiency of the power plant. CuCrZr exposed at temperatures above 400 ºC is susceptible of thermal softening due to over-ageing and suffers embrittlement under irradiation at temperatures below 200 ºC [1, 2, 5, 6]. Moreover, high strength DS Cu-Al_2O_3, as well as PH CuCrZr, exhibit important thermal creep at temperatures above ~ 350 ºC for applied stresses above 60 MPa [6, 7]. As the working temperature window established for these alloys under DEMO relevant conditions is quite narrow, i.e. 200 – 350 ºC [8], it would be very convenient to investigate the capabilities of other high-strength and heat-resistant Cu alloys that can exhibit a more favorable range of working temperatures, and retain a high thermal conductivity.

Among the second-phase particles that have been attempted to strength Cu, Y_2O_3 nanoparticles appear to have more potential than Al_2O_3 nanoparticles, since the

driving force for Y_2O_3 formation in Cu by internal oxidation (IO) is somewhat higher, the solubility and diffusivity for Y in Cu is lower than those for Al, and the lattice mismatch is significantly larger at Y_2O_3/Cu interfaces than at Al_2O_3/Cu interfaces [3, 9 – 11]. The last would imply a higher diffusional relaxation of the dislocation core stresses at the Y_2O_3/Cu interfaces, i.e. a more attractive particle-dislocation interaction, which can constrain the dislocation motion and enhance the mechanical strength at high temperature [12]. In fact, high stress creep measurements performed on DS Cu/Y_2O_3 yielded a relaxation parameter for the particle/dislocation interaction of k=0.82, against k≈0.9 for DS Cu/Al_2O_3, which points out to a stronger Y_2O_3-dislocation interaction and, therefore, a particular effect on the particle/matrix interface on the creep deformation [11, 13]. If this is the case, DS Cu/Y_2O_3 deformation processed under the same conditions as Cu/Al_2O_3, and with a particle dispersion equivalent to each other in size and volume fraction, could exhibit superior strength at elevated temperature.

Mechanical alloying is the traditional approach to attain a controlled and homogenous dispersion of nanoparticles in a metal matrix. In the case of a Cu matrix, cold welding of the powder particles during the high energy milling prevents the achievement of a suitable dispersion. It can be avoided by either cryogenic milling or addition of dispersing agents. Although cryogenic milling can give place to a dispersion of Y_2O_3 particles in Cu [14], it is an expensive method at industrial scale. Addition of dispersion agents, such as stearic acid, can produce a satisfactory dispersion of Y_2O_3 particles, but the powder must be, before consolidation, submitted to thermal treatment to remove the dispersion agent [15]. At present, these treatments do not appear to be effective for taking away satisfactorily the impurities resulting from the decomposition of the dispersion agent. Recently, a two-steps milling process has been applied to produce a dispersion of Y_2O_3 nanoparticles in Cu [16]. First Cu and Y elemental

powders are milled and a solid solution of Cu(Y) is obtained. Afterwards CuO powder is added and the blend suitably milled to induce the formation of Y_2O_3. However, the residual presence of CuO embrittles the consolidated alloy.

The present work is addressed to produce dispersion strengthened Cu-Y alloys via internal oxidation of the alloying element during high energy milling and subsequent HIP consolidation. The microstructure and mechanical characteristics of a Cu-1%Y alloy has also been investigated.

2. Experimental procedure

A homogenous blend with a target composition Cu-1%Y (wt%) was prepared mixing 99.97 % pure Cu and 99.9 % pure Y elemental powders for 4 h under a high purity Ar atmosphere in a Turbula T2F mixer. The Cu powder had particle sizes ranging from 3.8 to 138 μm, and the Y particle sizes were < 400 μm. The powders were purchased from Alfa Aesar. According to the manufacturer certificate of analysis the major impurity content in the Cu powder was 0.023 wt% of O, and Fe (430 ppm), Ca (429 ppm), Si (230 ppm) and rare earths (~ 10 ppm) in the Y powder. The blend was mechanically alloyed for 22 h under high purity Ar in a high-energy planetary mill using 5 mm Ø Cr steel balls as grinding media at a ball-powder weight ratio of 7:1. The milling process was done at 100 rpm alternating short milling periods of 120 seconds with rest periods of 180 seconds to prevent cold welding. The milled powder was canned in Ø 43 mm×80 mm steel canisters, degassed for 24 h at 573 K and vacuum-sealed. In each step of the procedure the powders were manipulated inside a glove box under Ar flow. The powder consolidation was accomplished by HIP treatment of the canisters for 2 hours at 1123 K and 179 MPa.

A consolidated ingot was shaped into 10×10×80 mm^3 billets and submitted to severe deformation by ECAP up to 4 passes at 623 K and a ramp rate of 0.333 mm/s following B_C route. Between the successive passes, this route changes the orientation of the billet respect the die axis by a rotation of +90º around its longitudinal axis. The intersection angle of the two channels was Φ = 105º with a curvature angle at the external intersection point of Ψ = 35º, which induced a homogeneous shear strain per pass estimated in $\gamma = 2.03$ resulting in an equivalent strain of $\varepsilon = 1.17$ per pass, see Fig. 1. To stabilize the microstructure of the ECAP deformed material, the billets were thermal treated for 2 h at 523 K in vacuum.

The size distribution of the powder particles was measured by the laser light scattering technique. The oxygen content after each processing step was determined by the combustion method in a LECO© analyzer. The X-Ray diffraction (XRD) patterns were analyzed by the Rietveld method using the Fullprof software [17] in order to determine the milling effects on the lattice parameters, crystallite sizes and the internal strains in the samples. The contribution of the diffractometer to the peak shapes was determined from a precise XRD pattern of a reference sample. The instrumental and the microstructure effects on the peak broadening were extracted applying the integral breadth analysis assuming a pseudo-Voigt function for the peak shapes and isotropic broadening for strain and crystallite size [18]. The microstructure of the milled powder and consolidated alloy were studied by optical microscopy (OM) and scanning electron microscopy (SEM) in a XL-30 PHILIPS microscope and in an ultra-high resolution imaging microscope TENEO FEI. The grain size distribution of the consolidated material was assessed from OM and SEM images applying an improved approach of the Jhonson-Saltykov stereological method [19]. The etchant used for revealing the grain structure was a 6 vol% HNO_3 solution in methanol. Crystallography macrotexture

measurements were carried out in a Siemens diffractometer equipped with a D5000 goniometer, on samples previously subjected to ECAP. The measurements were performed on samples cut perpendicular to the transverse direction (TD) of the billet (plane XY). The pole figures (1 1 1) were recorded over the azimuthal angle range $0° \leq \chi \leq 80°$.

The mechanical characterization was accomplished by Vickers microhardness measurements at room temperature and tensile tests, on samples ECAP deformed as well as on samples in the as-HIP condition. The microhardness measurements were performed on well-polished surfaces of samples cut parallel to the XY plane with an applied load of 9.81 N during 20 seconds, which were isothermally annealed for 2 h in pure Ar at temperatures in the range 293 – 773 K. The tensile tests were done on flat samples of 15 mm gauge length, 3 mm width and 1 mm thickness also cut parallel to the plane XY with their longitudinal axis along the extrusion direction (X axis). The tests were carried out through the temperature range 293 - 773 K at a constant strain rate of 1.1×10^{-4} s^{-1} under flowing Ar in a Shimadzu universal testing machine.

3. Results and discussion

3.1 Powder characterization

The evolution of the powder particle size and O content with milling time are shown in Figs. 2 and 3, respectively. Initially, most of the starting powder particles had sizes between 20 and 138 μm. After 2 h of milling the particle size distribution was shifted to the interval 240 – 1900 μm, and remained without visible changes even up to milling for 18 h. Although the milling process did not yield effective refinement of the

powder particle size, it produced dispersion of Y-rich particles in the Cu matrix, as the analyses of the microstructure presented in § 3.2. reveal. Moreover, the milling process increased the O content significantly, from 0.047 ± 0.002 wt % in the unmilled blend, up to 0.24 ± 0.01 wt % after milling for 2 h. Although the powder handling and milling were done under pure Ar, oxygen uptake occurred during milling likely coming from the grinding media and the jar walls. After the early milling stages, the powder particles turned into flaky shaped as Fig. 4 revealed. No bulky particle agglomeration was apparent under the present milling conditions.

Fig. 5 shows the milling effect on the X-ray diffraction patterns of Cu-1%Y powder. After milling for 2 h, diffraction peaks corresponding to Y_2O_3 are visible whereas those attributable to elemental Y powder are not detected. However, the Y_2O_3 peaks are no longer visible after milling for ≥ 6 h suggesting the virtual Y_2O_3 dissolution or amorphization induced by mechanical alloying. Since the increase of the oxygen content coincides with appearance of the Y_2O_3 phase, the initial formation of Y_2O_3 can be attributed to the oxidation of the fresh surfaces resulting from fragmentation of the starting Y particles during the early milling stage. It is worth noticing that if the total nominal content of Y atoms had transformed into Y_2O_3, the O content should have risen to ~0.27 wt %. Such an amount matches with the O content measured in the powder after milling for 2 h, see Fig. 3. After 2 h of milling, the O content varies around ~0.20 wt % up to the end of milling process, which could be attributed to a mutual O exchange among powder, grinding media and jar walls during milling. After the HIP consolidation, diffraction peaks attributable to Y_2O_3 reappear, suggesting that the HIP treatment induces Y_2O_3 reprecipitation. It is worth noticing that the O content decrease to 0.121 ± 0.006 wt % is due to the effective degassing treatment of the powder before consolidation.

The effects of the milling process in the crystallite size, internal strain and lattice parameters are shown in Fig. 6. The crystallite size steeply decreases after 2 h of milling and remains constant after 10 hours of milling. The internal strain increases with increasing milling time without clear evidence of strain saturation in the powder particles. In addition, the lattice parameter shows a weak increasing trend with increasing milling time that could be correlated to the solution of Y in the Cu matrix, in agreement with the reported results for Cu-Y and Cu-Al alloys [16, 20].

3.2. Microstructure

3.2.1. As-HIP condition

The consolidated alloy resulted in a fully dense material since its density measured in a He ultra-pycnometer was 8.78±0.04 g/cm^3, very close to the calculated value for the nominal composition applying the mixing rule, i.e. 8.851 g/cm^3. Furthermore, evidence of residual pores was not found in the optical and SEM images. A general view of the microstructure in the as-HIP condition is shown in Fig. 7. A banded grain structure composed of very elongated bands evidences its formation by the cold-welding phenomena between powder particles during the milling. The bands appear to be composed of small grains and delimited by prior particle boundaries (PPBs) replicating the flaky morphology of the milled particles.

The BSE-SEM images shown in Fig.8 reveal the typical presence of Y oxide particle strings developed at what presumably were PPBs. Fig. 8b shows that these large Y oxide particles are not located along the grain boundaries. In contrast, the nanosized particles can be found at the grain and subgrain boundaries, as well as inside the recrystallized grains. The large Y oxide particles forming the long strings observed, i.e.

the particles with sizes around 1 - 2 μm, usually exhibit a polygonal habit, and coarsen by coalescence as Fig. 8c reveals. The EDX analyses of the large particles aligned in strings, see Fig. 8d, indicated a Y/O ratio compatible with the Y_2O_3 composition. Fig. 9 shows the characteristic microstructure induced by recrystallization consisting of small equiaxed grains with bulged boundaries, which contain inside Y-rich particles. The regions with smaller grains contain a very high number density of these particles while those with grain sizes significantly larger exhibit a very low number density, as Fig. 9 shows.

The frequency and volume grain size distributions of ~2000 grains are represented in Fig. 10. From these data, a mean grain size of 1.8 ± 1.4 μm was obtained. The sizes of more than 1500 Y-rich particles were also measured on electron channeling contrast (ECC) images from different areas of the samples. Fig. 11 shows the particle size distribution along with the corresponding volume distribution. This size distribution, which is apparently bimodal with modal values at 50 nm and 100 nm, yields a mean particle diameter of 99 ± 9 nm. The volume distribution gives a cube root of the mean cube particle diameter of $\sqrt[3]{\langle d^3 \rangle} = 218 \pm 20$ nm. The total volume fraction of particles in the sample resulted in 1.98±0.05 %, in good agreement with the value of 2.2 % calculated assuming that the nominal content of Y is completely transformed into Y oxide particles.

3.2.2. ECAP deformed

Fig. 12 shows general views of the material after being ECAP deformed for 4 B_C passes at 623 K and subsequently heat treated at 523 K. The ECC images, compared with the corresponding for the as-HIP material, reveal no qualitative differences in the grain microstructure and particle distribution irrespective of the observation plane. The

large particles also appear aligned in strings, and the small ones distributed inside the grains as well as at the grain boundaries. Likewise it occurs in the as-HIP condition, the particles are not found homogeneously distributed, and regions with higher number density of particles exhibit smaller grain sizes. The ECAP deformation appears to reduce the grain size to a mean value of 1.3 ± 0.9 μm as Fig. 10 shows. Furthermore, the ECAP processing induced an evident refinement of the particle dispersion resulting in a mean particle size of 58 ± 8 nm, as the size distribution shows in Fig. 11.

In order to investigate the stability of the ECAP-induced microstructure a study of the crystallography macrotexture evolution was done on samples in the as-HIP condition and subsequently annealed for 1 h at 773 K. Prior to ECAP processing, the material did not exhibit any crystallographic texture, because the powder metallurgy production route used to obtain the Cu-1%Y ingots results in a random grain orientation. Fig. 13a shows the experimental incomplete (1 1 1) pole figure after ECAP, measured in the flow plane perpendicular to the transverse direction (z-TD). As reference, the ideal texture components for simple shear deformation of a fcc material are displayed on the same figure [21]. The ideal crystallographic textures have been represented in the simple shear $x'y'z$ reference system as the plane-direction pair $\{h\ k\ l\}\langle u\ v\ w\rangle$, where $\{h\ k\ l\}$ corresponds to a plane parallel to the y'-plane and $\langle u\ v\ w\rangle$ to a direction parallel to the x' axis. A clockwise rotation of $\Phi/2$ around the z axis changes from the simple shear reference system $x'y'z'$ to the laboratory system xyz. After ECAP, the observed weak texture can be ascribed to the presence of a C texture component $\{0\ 0\ 1\}\langle 1\ 1\ 0\rangle$, along with the components $B/\overline{B}\ (1\ \bar{1}\ 2)[1\ 1\ 0]/(\bar{1}\ 1\ \bar{2})[\bar{1}\ \bar{1}\ 0]$ and $A/\overline{A}\ (1\ \bar{1}\ 1)[1\ 1\ 0]/(\bar{1}\ 1\ \bar{1})[\bar{1}\ \bar{1}\ 0]$. This observed texture agrees with those reported by several authors for pure Cu processed via route B_C [21 – 23].

However, the spread of the (1 1 1) intensity is wider than the corresponding to an ideal simple shear deformation, due to the internal angle $\Psi = 35°$ of the ECAP die deviates the applied strain from a simple shear deformation to a process with a continuous distribution of shear planes. After annealing at 773 K the measured pole figure (1 1 1) showed a global decrease in the texture intensity as Fig. 12b reveals, in agreement with the results reported by several authors for pure copper annealed at temperatures above 773 K [23 – 26].

3.3 Mechanical properties

The microhardness measurements performed on longitudinal and transversal sections of the billets did not reveal anisotropy. The effect of the thermal treatments on the microhardness value at room temperature is shown in Fig. 14. The material in the as-HIP condition exhibits a microhardness value of 900 ± 40 MPa, remaining nearly constant after heat treatments at T≤773 K. The ECAP processing produced a remarkable increase in the microhardness, to a value of 1230 ± 40 MPa, which was maintained constant up to the heat treatment at 573 K. This value coincides with those reported for GlidCop® Al25 in the as-extruded condition, 1206 MPa, and for CuCrZr-ITER in the aged after cold-working condition, 1226 MPa. For temperatures higher than the ECAP one (623 K) the microhardness value drops. These results evidence the microhardness increase is due to grain refinement, and its reduction is attributable to static recovery and recrystallization of the ECAP deformed microstructure.

Fig. 15 shows the engineering stress-strain curves for the material in the as-HIP and ECAP deformed conditions. Their tensile characteristics given by the yield strength σ_Y (0.2 % true stress), ultimate tensile stress σ_{UTS} and the uniform true plastic strain ε_U, as a function of temperature, are represented in Fig. 16. The tensile curves of the as-HIP

alloy exhibit the characteristic behavior of pure Cu: a strengthening by plastic deformation, and an increase of the ductility along with a diminution of the mechanical strength on increasing the temperature.

ECAP deformation enhances the mechanical strength and reduces the ductility. At 573 K the ECAP deformed samples exhibit a limited strain hardening, a reduced uniform strain and a pronounced softening indicating changes in the microstructure due to dynamic recrystallization. In contrast, the microstructure of the as-HIP samples still appear to be stable at 573 K, although their microstructures cannot be maintained at 773 K, as suggests the softening observed for these samples in Fig. 15.

In order to optimize the processing conditions of this alloy and predict its performance during service, the flow stress and work hardening behavior have been analyzed in term of the Voce law given by the relationship [27]:

$$\sigma = \sigma_s - (\sigma_s - \sigma_o)\exp\left(-\frac{\varepsilon_{pl}}{\varepsilon_C}\right) \quad (1)$$

where ε_{pl} is the true plastic strain, σ_S the saturation flow stress, σ_o the flow stress at ε_{pl} =0, and ε_C the corresponding critical plastic strain at σ_S. From the fits of the experimental true stress and true plastic strain values, i.e. σ and $\varepsilon_{pl,}$ to eq. (1), the predicted Voce parameters σ_o, σ_s and ε_c were obtained. The respective correlations between the predicted Voce parameters, σ_o, σ_s and $\varepsilon_{UTS,Voce}$ and the σ_y, σ_{UTS} and ε_{UTS} values, determined from the experimental true σ-ε curves, are shown in Fig. 17. The uniform true plastic strain predicted by Voce relationship, $\varepsilon_{UTS,Voce}$, was calculated imposing the condition $d\sigma/d\varepsilon_{pl} = \sigma_S$ to eq. (1).

The predicted parameters match very satisfactorily with the ones obtained from the experimental data except for the data points corresponding to σ_{UTS} and ε_{UTS} measured at 293 K, see Figs. 17b and c. It is worth noticing in the engineering stress-strain curve for the as-HIP material at 293 K that the sample failed before attaining a maximum stress. Then, the σ_{UTS} and ε_{UTS} values obtained for this sample from the true σ-ε curves do not really correspond to the stated parameters. The variation of the critical plastic strain values ε_c with temperature is represented in Fig. 18 along with the ε_{UTS} and $\varepsilon_{UTS,Voce}$ values. For the ECAP deformed material these values are practically independent of the temperature in the investigated range. Fig. 19 depicts the flow stress at different given plastic deformations, as a function of temperature. The temperature dependence of the flow stress turns out to be virtually linear when steady state deformation is attained, as the normalized values of the saturation stress σ_s versus the normalized temperature show in Fig. 20; the stress values are normalized by the temperature dependent shear modulus μ (T) for pure Cu given in Ref. [28].

The temperature dependence of the flow stress may be predicted from the dependence of the shear strain rate $\dot{\gamma}$ at a particular stress and temperature, which is given by an Arrhenius law [29]

$$\dot{\gamma} = \dot{\gamma}_o \exp\left(-\frac{\Delta H}{kT}\right) \qquad (2)$$

where ΔH is the activation enthalpy, k the Boltzmann constant, T the temperature and $\dot{\gamma}_o = \gamma_o t_w^{-1}$; here γ_o is the shear strain consequent to surpass the obstacle and t_w the dislocation waiting time for surpassing it. The appropriate stress and temperature dependence of ΔH and γ_o have to be established to predict a reliable temperature dependence of the flow stress. When an effective resolved shear stress τ_{eff} acts on a

mobile dislocation pinned by a discrete obstacle, the activation enthalpy would be given by

$$\Delta H = \Delta U - \left(\tau - \tau_i\right) V^* \qquad (3)$$

where ΔU is the activation energy, $\left(\tau - \tau_i\right) = \tau_{eff}$ and $V^* = \Delta A\, b$ the activation volume; τ is the applied resolved shear stress, τ_i is the temperature-independent back stress due to the long-range stress field of the dislocations, ΔA is the swept area by the dislocation and b is the Burger vector modulus. Inserting eq. (3) in eq. (2), and considering relationships of γ and τ with the tensile strain ε and tensile stress σ through the Taylor factor M_T, the temperature dependence of the applied tensile stress would be given by the equation:

$$\sigma = \left(\sigma_i + \frac{M_T}{V^*}\Delta U\right) - \frac{M_T}{V^*}\ln\left(\frac{\dot{\varepsilon}_o}{\dot{\varepsilon}}\right)kT \qquad (4)$$

The results shown in Fig. 19 exhibit a non-linear temperature dependence of σ indicating that some of the parameters σ_i, ΔU, V^* and ε_o would depend on σ or/and T. Nevertheless, Fig. 20 reveals that the saturation stress values σ_s, and therefore the measured σ_{UTS} values, exhibit an acceptable lineal temperature dependence irrespective of whether the samples were tested in the as-HIP or ECAP deformed conditions. The fit of the point data brings about

$$\left(\sigma_i + \frac{M_T}{V^*}\Delta U\right)\Bigg|_{steady-state} = \left(12.1 \pm 0.3\right) \times 10^{-3}\,\mu_o \qquad (5)$$

where μ_o is the shear modulus at 0 K, and a slope value

$$\left.\frac{M_T}{V^*/b^3}\ln\left(\frac{\dot{\varepsilon}_0}{\dot{\varepsilon}}\right)\right|_{steady-state} = 0.49 \pm 0.03 \qquad (6)$$

One can determine the V^* using the Taylor factor for textureless Cu, M_T=3.06, the applied strain rate $\dot{\varepsilon} = 1.1\times10^{-4}$ s^{-1} and an appropriate $\dot{\varepsilon}_o$. The last parameter can be extracted from $\dot{\gamma}_o = \gamma_o t_w^{-1}$ using the values reported for Cu, i.e. $\gamma_o \approx 10^{-4}$ and $t_w^{-1} \approx 10^{11}$ s^{-1}, which have been satisfactorily applied [29, 30]. It should be noted that these parameters would not be directly measurable, and the samples in the as-HIP or ECAP deformed conditions exhibited so weak crystallography texture that the Taylor factor for a random distribution of grain orientations may be applied for the present fits. Thus, using $\left(\dot{\varepsilon}_o/\dot{\varepsilon}\right) \cong 10^{11}$, the V^* value for steady state deformation results in $155b^3$. This value is consistent with the one of ~$135b^3$ reported for ultra-fine crystalline (UFC) Cu with grain size of 500 nm and accumulative roll bonding (ARB) Cu, and attributed to dislocation climb in Cu [31, 32].

The expected flow stress σ at 0 K, i.e. $\left.\left(\sigma_i + \frac{M_T}{V^*}\Delta U\right)\right|_{steady-state}$, should correspond to the mechanical threshold above which plastic flow can take place without thermal activation. This value would represent the maximum deformation resistance of the material. This value is about 540 MPa for the Cu-1Y samples processed under the present conditions.

The tensile strain hardening rates calculated from experimental σ-ε_{pl} curves, i.e. $\Theta = \left(d\sigma/d\varepsilon\right)$ normalized by $\mu(T)$, as a function of the normalized flow stress $\left(\sigma/\sigma_S\right)$, are represented in Fig. 21. The plots indicate that after the fast initial decrease of Θ, the as-HIP samples tested at RT, 373 and 573 K exhibit the characteristic linear behavior of

the stage III work hardening observed in f.c.c. metals and ferritic steels [27, 30]. This behavior may be fitted by the equation

$$\Theta = \Theta_o \left(1 - \frac{\sigma}{\sigma_S} \right) \qquad (7)$$

giving a slope of $\Theta_o \approx 0.09\mu$, which is compatible with the fitted Voce equations. Neither the as-HIP sample tested at 773 K nor the samples ECAP processed exhibit this typical Stage III behavior, but only the fast initial drop attributed to transient stage where several competing mechanisms could be active. In fact, the ECAP deformed material tested at RT and 373 K exhibits the same hardening behavior that the as-HIP material tested at 773 K, see Fig. 21.

4. Conclusions

A Cu-1Y alloy containing a dispersion of submicrometric Y oxide particles has been developed. Cold welding during mechanical alloying was effectively inhibited using short milling periods alternated with long rest periods favoring the Y dissolution in the Cu matrix, and the formation of a Y-rich particle dispersion after the powder consolidation by HIP. The study of the microstructure and mechanical characteristics of this alloy in the as-HIP and ECAP deformed conditions provides the following conclusions:

1. The particle dispersion exhibited a bimodal distribution of sizes with a mean size of 99 nm. It has been demonstrated that the ECAP processing can homogenize and refine the particle dispersion to a mean particle size of 58 ± 8 nm. EDS analyses of

the particles reveal a composition compatible with Y_2O_3. The total volume fraction of these particles in the alloy resulted in 1.98 %.

2. The microhardness measurements and the tensile tests have demonstrated the capability of this dispersion to enhance the strength of a Cu matrix. The ECAP deformation induced an improvement of the tensile strength respect to the alloy in the as-HIP condition. This improvement disappears at temperatures ≥ 573 K due to dynamical recovery. The ductility decline for the ECAP deformed alloy is maintained above this temperature.
3. It is found that the plastic and work hardening behavior of this alloy, at a strain rate of ~10^{-4} s^{-1} in the temperature range 293 – 773 K, is quite well described by the Voce law. The Voce parameters obtained from the fits of the experimental data match to the corresponding experimental measurements for yield strength, uniform strain and ultimate tensile stress. The strain hardening rate plots as a function of flow stress for the samples tested at 293 ≤ T ≤ 773 K exhibited a two-stage behavior. In these cases, it comprises a transient stage at low stresses, with fast decreasing hardening rate with increasing stress, followed by the characteristic linear dependence for the stage III of hardening in f.c.c. metals. The ECAP deformed alloy only exhibited the transient stage.
4. The σ_{UTS} and σ_s values for the samples tested in the as-HIP and deformed conditions exhibit a linear dependence on temperature. From these data the activation volume for the steady-state plastic deformation have been assessed in $155b^3$.

Acknowledgements

The present work has been supported by the Ministerio de Economía y Competitividad of Spain (ENE2015-70300-C3-2-R MINECO/FEDER) and by the Regional Government of Madrid through the programs S2013/MAE-2745 TECHNOFUSION(II)-CM and S2013/MIT-2862-MULTIMAT-CHALLENGE.

References

[1] S.J. Zinkle, Applicability of copper Alloys for DEMO high heat flux components, Phys. Scr. T167 (2016) 014004 (10 pp).

[2] J.H. You, Copper matrix composites as heat sink materials for water-cooled divertor target, Nucl. Mater. Energy 5 (2015) 7 – 18.

[3] J.R. Groza, J. C. Gibeling, Principles of particle selection for dispersion-strengthened copper, Mater. Sci. Eng. A 171 (1993) 115 – 125.

[4] D. Stork et al., Materials R&D for a timely DEMO: Key findings and recommedations of the EU Roadmap Materials Assessment Group, Fusion Eng. Des. 89 (2014) 1586 – 1594.

[5] S.A. Fabritsiev, S.J. Zinkle, B.N. Singh, Evaluation of copper alloys for fusion reactor divertor and first wall components, J. Nucl. Mater. 233-237 (1996) 127 – 137.

[6] M. Li, S.J. Zinkle, Physical and Mechanical Properties of Copper and Copper Alloys, Comprehensive Nuclear Materials 4 (2012) 667 – 690.

[7] G. Li, B.G. Thomas, J.F. Stubbins, Modeling Creep and Fatigue of Copper Alloys, Metall. Mater. Trans. 31A (2000) 2491 – 2502.

[8] D. Stork et al., Developing structural, high-flux and plasma facing materials for a near-term DEMO fusion power plant: The EU assesment, J. Nucl. Mater. 455 (2014) 277 – 291.

[9] M.S. Nagorka, C.G. Levi, G.E. Lucas, S.D. Rider, The potential of rapid solidification in oxide-dispersion-strengthened copper alloy development, Mat. Sci. Eng. A142 (1991) 277 – 289.

[10] M.S. Nagorka, C.G. Levi, G.E. Lucas, Novel Oxide-Dispersion-Strengthened Copper Alloys from Rapidly Solidified Precursors: Part 1, Metall. Mat. Trans. A 26A (1995) 859 – 871.

[11] M.S. Nagorka, C.G. Levi, G.E. Lucas, Novel Oxide-Dispersion-Strengthened Copper Alloys from Rapidly Solidified Precursors: Part 2, Metall. Mat. Trans. A 26A (1995) 873 – 881.

[12] J. Rösler, E. Artz, A new model-based creep equation for dispersion strengthened materials, Acta Metall. Mater. 38 (1990) 671 – 683.

[13] S.E. Broyles, K.R. Anderson, J.R. Groza, J.C. Gibeling, Creep Deformation of Dispersion-Strengthened Copper, Metall. Mater. Trans. A 27A (1996) 1217 – 1227.

[14] G. Carro, A. Muñoz, M.A. Monge, B. Savoini, R. Pareja, C. Ballesteros, P. Adeva, Fabrication and characterization of Y_2O_3 dispersion strengthened copper alloys, J. Nucl. Mater. 455 (2014) 655 – 659.

[15] S.M.S. Aghamiri, N. Oono, S. Ukai, R. Kasadb, H. Noto, Y. Hishinuma, T. Muroga, Microstructure and mechanical properties of mechanically alloyed ODS copper alloy for fusion material application, Nuclear Materials and Energy 15 (2018) 17-22.

[16] B. Huanga, Y. Hishinuma, H. Noto, R. Kasada, N. Oono, S. Ukai, T. Muroga, In-situ fabrication of yttria dispersed copper alloys through MA-HIP process, Nuclear Materials and Energy 16 (2018) 168-174.

[17] J. Rodríguez-Carvajal, Recent advances in magnetic structure determination by neutron powder diffraction, Physica B, 192 (1993) 55.

[18] D. Martínez-Blanco, P. Gorria, J.A. Blanco, M.J. Pérez, J. Campo, Analysis of the diffraction-line broadening on nanostructured Fe: size–strain effects induced by milling and heating J. Phys. : Condens. Matter 20 (2008) 335213 (10 pp).

[19] Y.H. Xu, H.C. Pitot, Computer Methods and Programs in Biomedicine 72 (2003) 1 – 20.

[20] T. Yamada, H. Noto, Y. Hishinuma, T. Muroga, H. Nakamura, Development of a dispersion strengthened copper alloy using a MA-HIP method, Nuclear Materials and Energy 9 (2016) 455–458.

[21] Saiyi Lia, Irene J. Beyerlein, Mark A.M. Bourke, Texture formation during equal channel angular extrusion of fcc and bcc materials: comparison with simple shear, Materials Science and Engineering A 394 (2005) 66–77.

[22] F.H. Dalla Torre, A.A. Gazder, E.V. Pereloma, Ch.H.J. Davies, Recent progress on the study of the microstructure and mechanical properties of ECAE copper, J Mater Sci 42 (2007) 9097–9111.

[23] X. Molodov, G. Gottsteina, M. Winning, R.J. Hellmig, Thermal stability of ECAP processed pure copper, Materials Science and Engineering A 460–461 (2007) 204–213.

[24] L.S. Toth, J.J. Jonas, D. daniel and J.A. Bailey, Textures and Microstructures, 1992, Vol. 19, pp. 245-262.

[25] M. Haouaoui, K.T. Hartwig, E.A. Payzant, Effect of strain path on texture and annealing microstructure development in bulk pure copper processed by simple shear, Acta Materialia 53 (2005) 801-810.

[26] S. Ferrasse, V.M. Segal, F. Alford, Texture evolution during equal channel angular extrusion (ECAE): Part II. An effect of post-deformation annealing, Materials Science and Engineering A 372 (2004), 235-244.

[27] G. Sainath, B.K. Choudhary, J. Christopher, E. Isaac Samuel, M.D. Mathew, Applicability of Voce equation for tensile flow and work hardening behaviour of P92 ferritic steel, Int. J. Pres. Ves. Pip. 132-133 (2015) 1–9.

[28] H.J. Frost, M.F. Ashby, Deformation-mechanism maps: the plasticity and creep of metals and ceramics, Pergamon press, (1982).

[29] U.F. Kocks, A.S. Argon, M.F. Ashby, Thermodynamics and Kinetics of Slip, Prog. Mater. Sci. 19 (1975).

[30] U.F. Kocks, H. Mecking, Physics and phenomenology of strain hardening: the FCC case Prog. Mater. Sci. 48 (2003) 171–273.

[31] L. Lu, R. Schwaiger, Z.W. Shan, M. Dao, K. Lu, S. Suresh, Nano-sized twins induce high rate sensitivity of flow stress in pure copper, Acta Mater. 53 (2005) 2169–2179.

[32] T. Kunimine, N. Takata, N. Tsuji, T. Fujii, M. Kato, S. Onaka, Temperature and Strain Rate Dependence of Flow Stress in Severely Deformed Copper by Accumulative Roll Bonding 50 (2009) 64–69.

Figure Captions

Figure 1. Schematic view of the ECAP process. The normal (ND), transverse (TD) and extrusion directions (ED) are indicated.

Figure 2. Particle size distribution of the powder during the milling process.

Figure 3. Evolution of the oxygen content with the milling time. The oxygen content of the specimen after consolidation by HIP is also displayed.

Figure 4. SEM image of the powder particles after 18 hours of milling.

Figure 5. X-Ray diffraction patterns of the powder after 2 and 22 h of milling and after consolidation by HIP.

Figure 6. Evolution of some crystallographic parameters with the milling time. (a) The crystallite size and strain. (b) Lattice parameter.

Figure 7. General view of the microstructure of Cu-1Y in the as-HIP condition. Optical Microscope image of a sample etched for revealing the grain structure.

Figure 8. (a) and (b) ECC images of Cu-1Y in the as-HIP condition showing the distribution of Y-rich particles. (c) Large yttrium-oxide particles in the long strings. (d) EDX diagrams obtained in the matrix (black line) and in a large yttrium-oxide particle (red line).

Figure 9. BSE/SEM images of the as HIP alloy showing the effects of the recrystallization during the consolidation.

Figure 10. Grain size distribution obtained from Optical Microscope images. (a) Grain size frequencies, As-HIP: shaded bar without lines, ECAPed: line-shaded bar. (b) Volume fraction, As-HIP: shaded bar without lines, ECAPed: line-shaded bar.

Figure 11. Size distribution of the Y-rich particles. (a) Particle size frequency versus particle size. As-HIP: shaded bar without lines, ECAPed: line-shaded bar. (b) Particle volume fraction versus particle size. As-HIP: shaded bar without lines, ECAPed: line-shaded bar.

Figure 12. ECC images of Cu-1Y showing the microstructure after the ECAP process. (a) General view showing the presence of Y-rich particles with a micrometer size and grains with different sizes. (b) Sub-micrometer Y-rich particles located both in the grain boundaries and inside the grains.

Figure 13. (1 1 1) experimental incomplete pole figures: (a) ECAPed samples after 4 passes following the B_C route and (b) after subsequent thermal treatment at 773 K for 1.5 h. The main ideal orientations (symbols) and partial fibers (black thick line) of simple shear deformed FCC materials are depicted in (a) for reference. The meaning of the symbols are indicated in the table.

Figure 14. Effect of the heat treatment on the room temperature microhardness of Cu-1Y in the as-HIP condition (solid circles) and ECAP deformed (open circles).

Figure 15. Engineering stress-strain curves for Cu-1Y in the as-HIP condition and ECAP deformed, at different temperatures.

Figure 16. Yield strength σ_Y, ultimate tensile stress σ_{UTS} (a) and the uniform true plastic strain ε_U (b) as a function of temperature for Cu-1Y in the as-HIP condition and ECAP deformed.

Figure 17. Correlation between the values σ_o, σ_S and ε_{Upred} predicted by the Voce law and the measured σ_Y, σ_{UTS} and ε_{UTS} values. (a) Flow stress σ_o compared to the experimental yield strength σ_{YS}. (b) Saturation flow stress σ_s compared to the

experimental Ultimate Tensile Strength σ_{UTS}. (c) Ultimate Tensile Strain according to the Voce model, $\varepsilon_{UTS,\,Voce}$ compared to the experimental ε_{UTS}.

Figure 18. Temperature dependence of different plastic strain parameters for Cu-1Y in the as-HIP condition and ECAP deformed.

Figure 19. Temperature dependence of the flow stress at fixed plastic strain values for Cu-1Y in the as-HIP condition (solid symbols) and ECAP deformed (open symbols).

Figure 20. Temperature dependence of the saturation stress σ_s calculated from the Voce model for Cu-1Y in the as-HIP condition (solid symbols) and ECAP deformed (open symbols). Both the saturation stress and the abscissa KT have been normalized by the shear modulus μ(T) of pure copper.

Figure 21. Strain hardening (normalized by the shear modulus of pure copper) as a function of the flow stress (normalized by the Voce saturation stress) for Cu-1Y in the as-HIP condition (solid symbols) and ECAP deformed (open symbols).

Figure1

Click here to download high resolution image

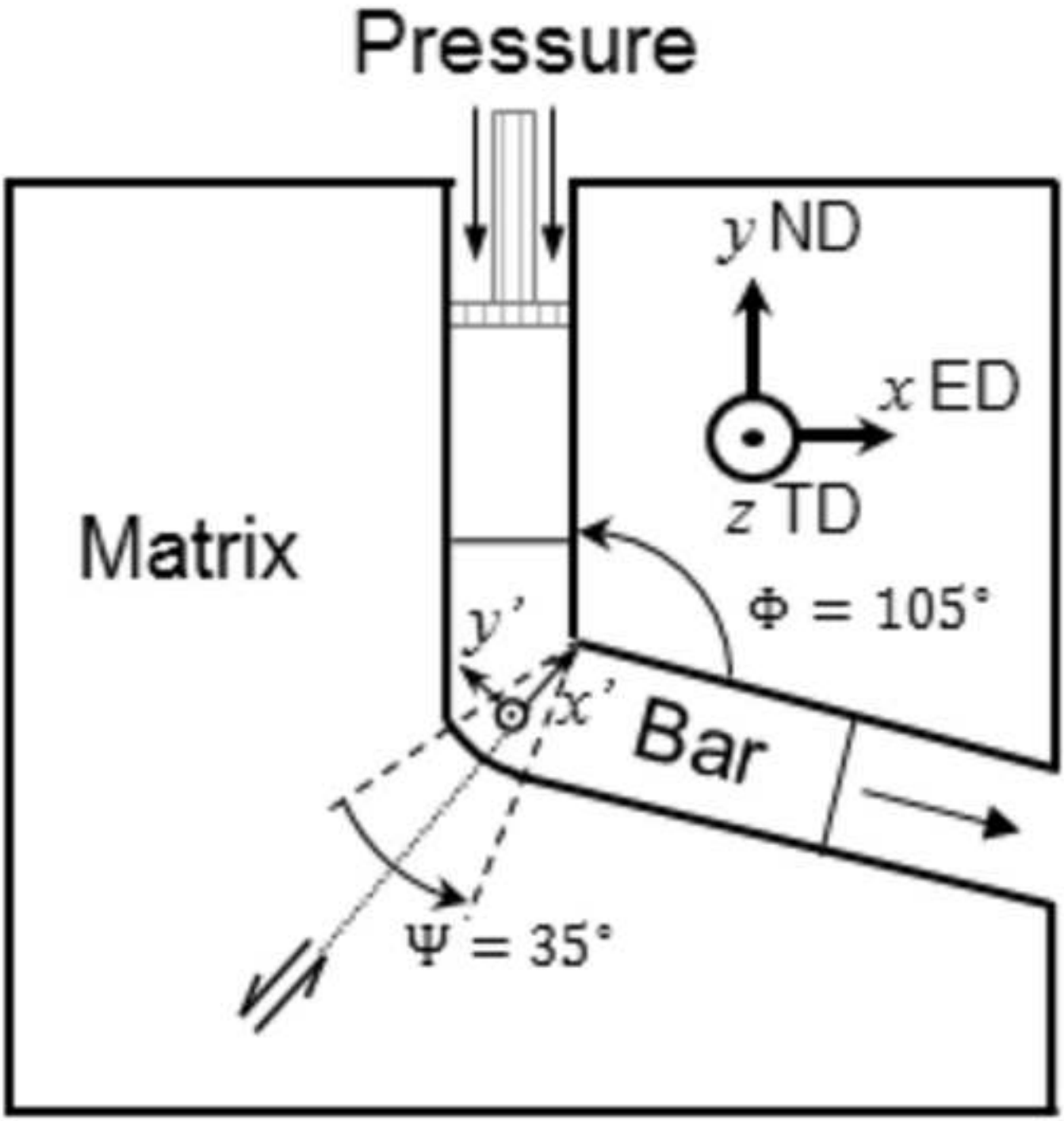

Figure2
Click here to download high resolution image

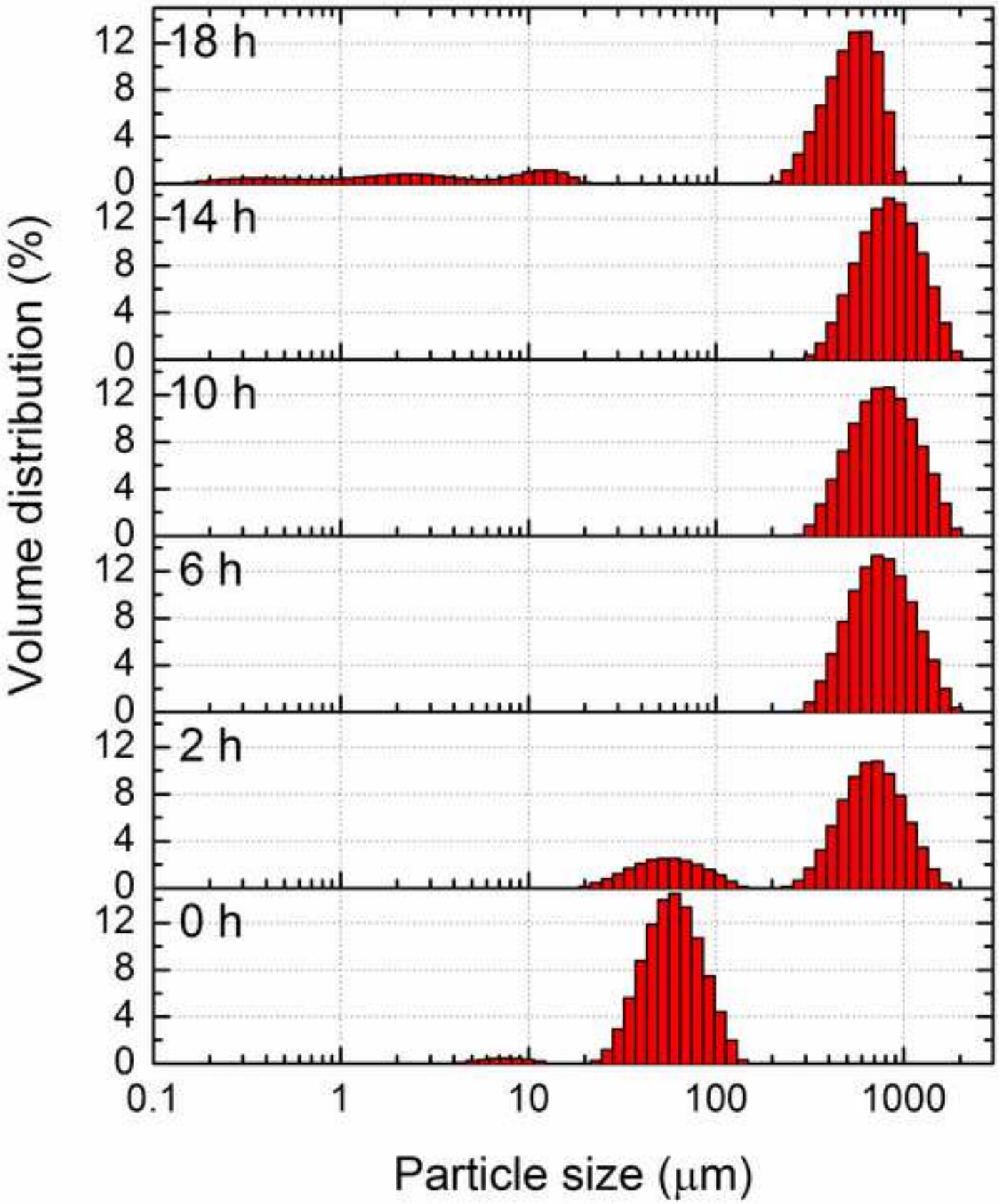

Figure3
Click here to download high resolution image

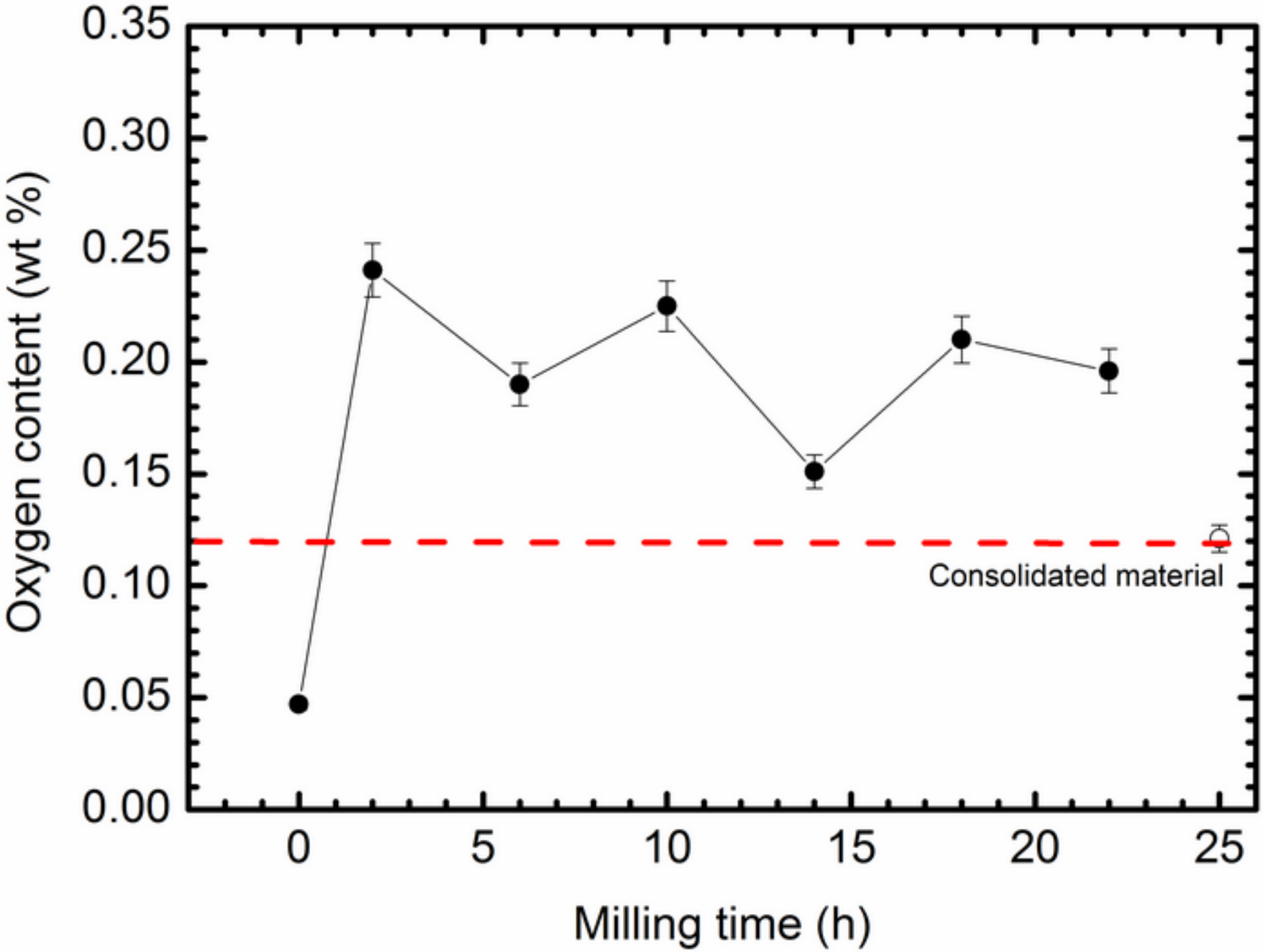

Figure4
Click here to download high resolution image

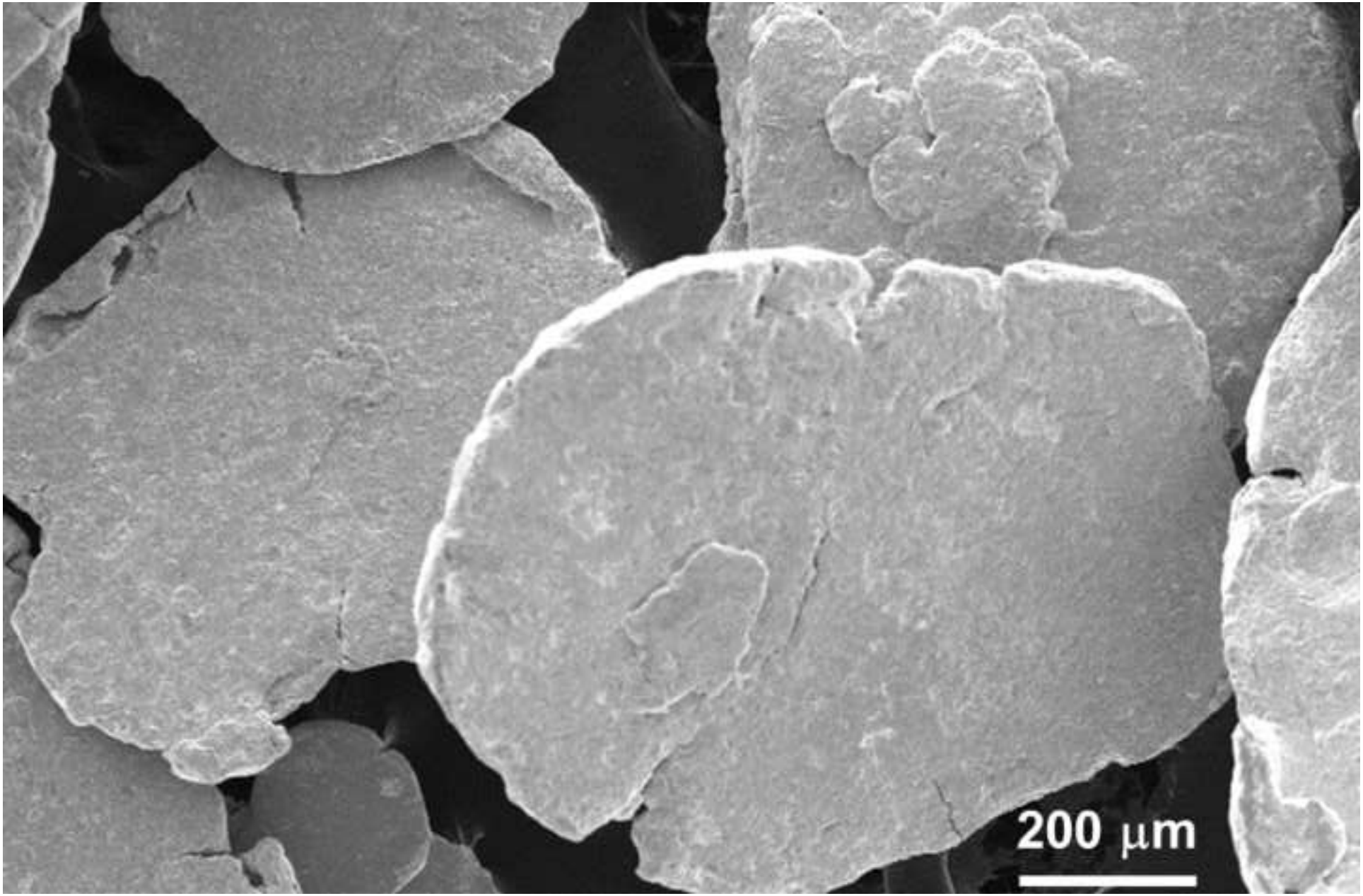

Figure5
Click here to download high resolution image

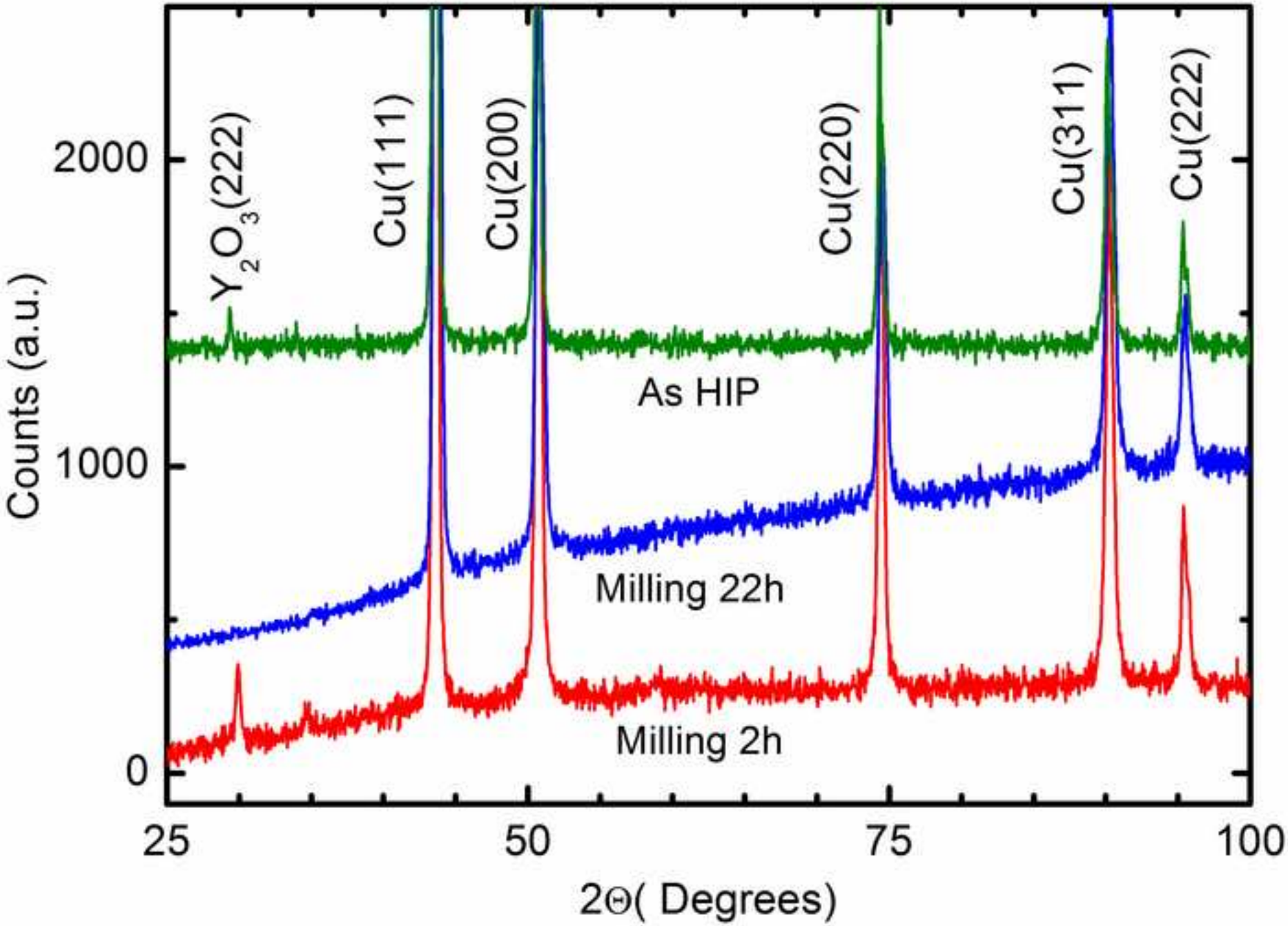

Figure6
Click here to download high resolution image

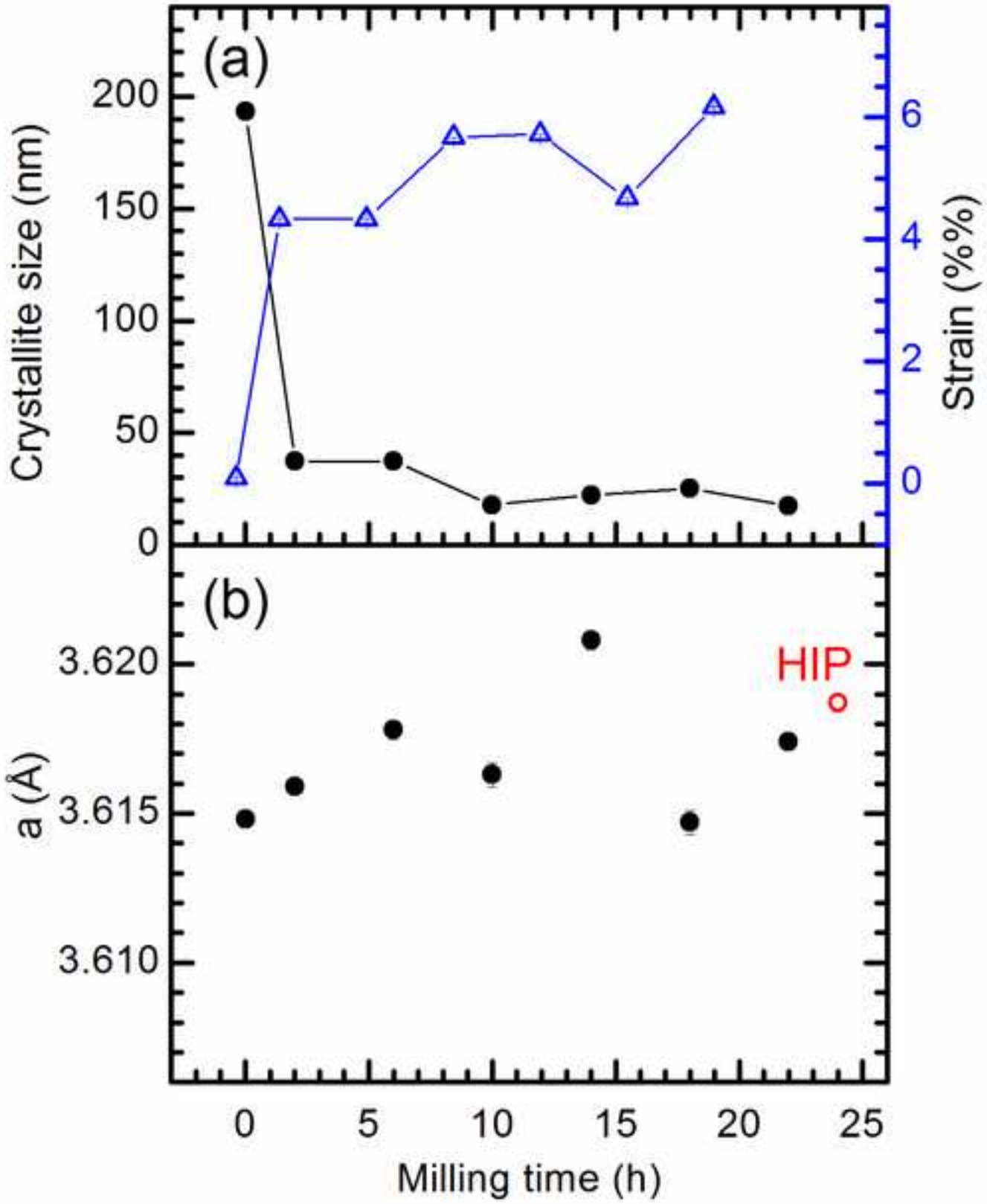

Figure7
Click here to download high resolution image

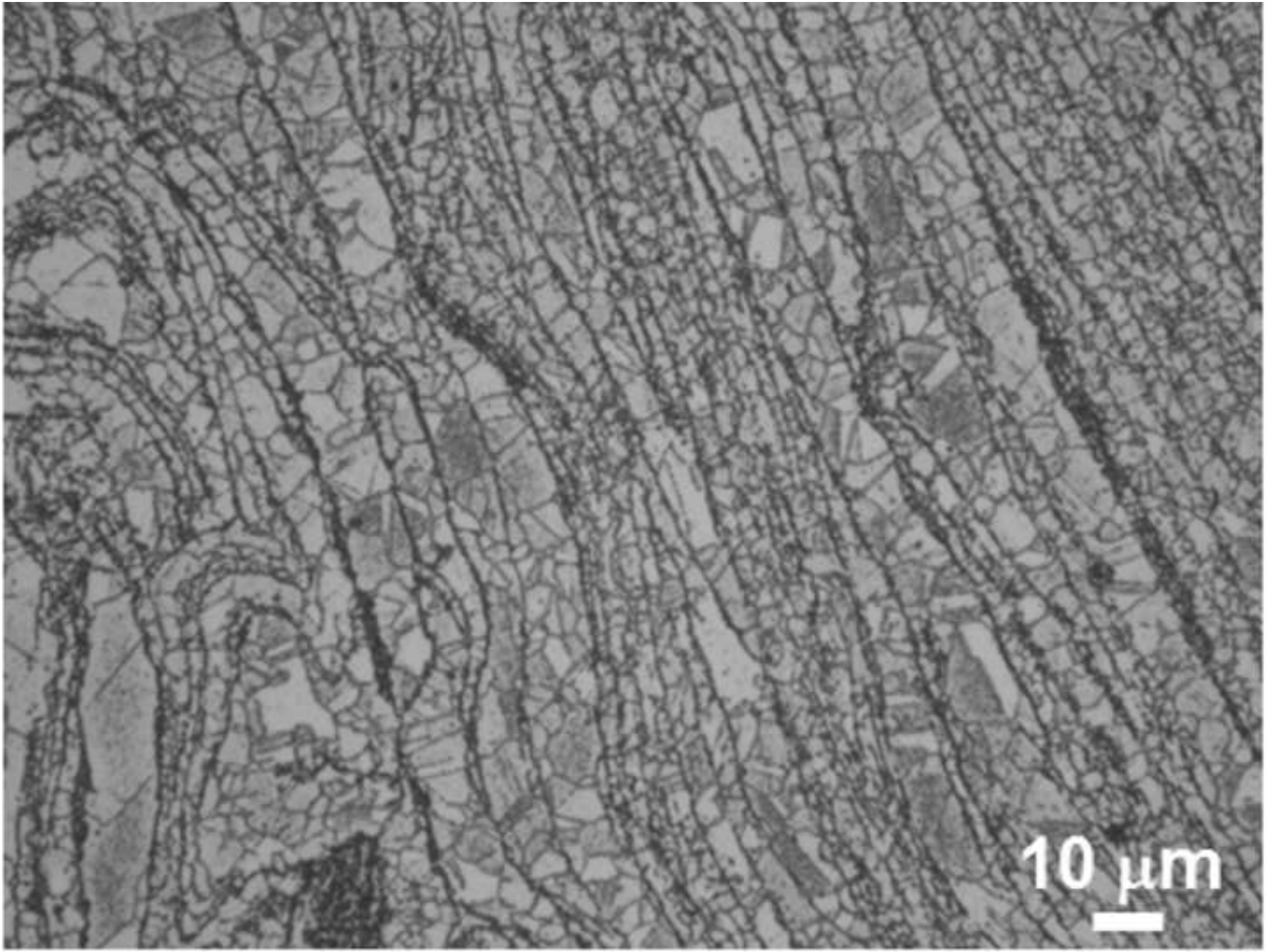

Figure8
Click here to download high resolution image

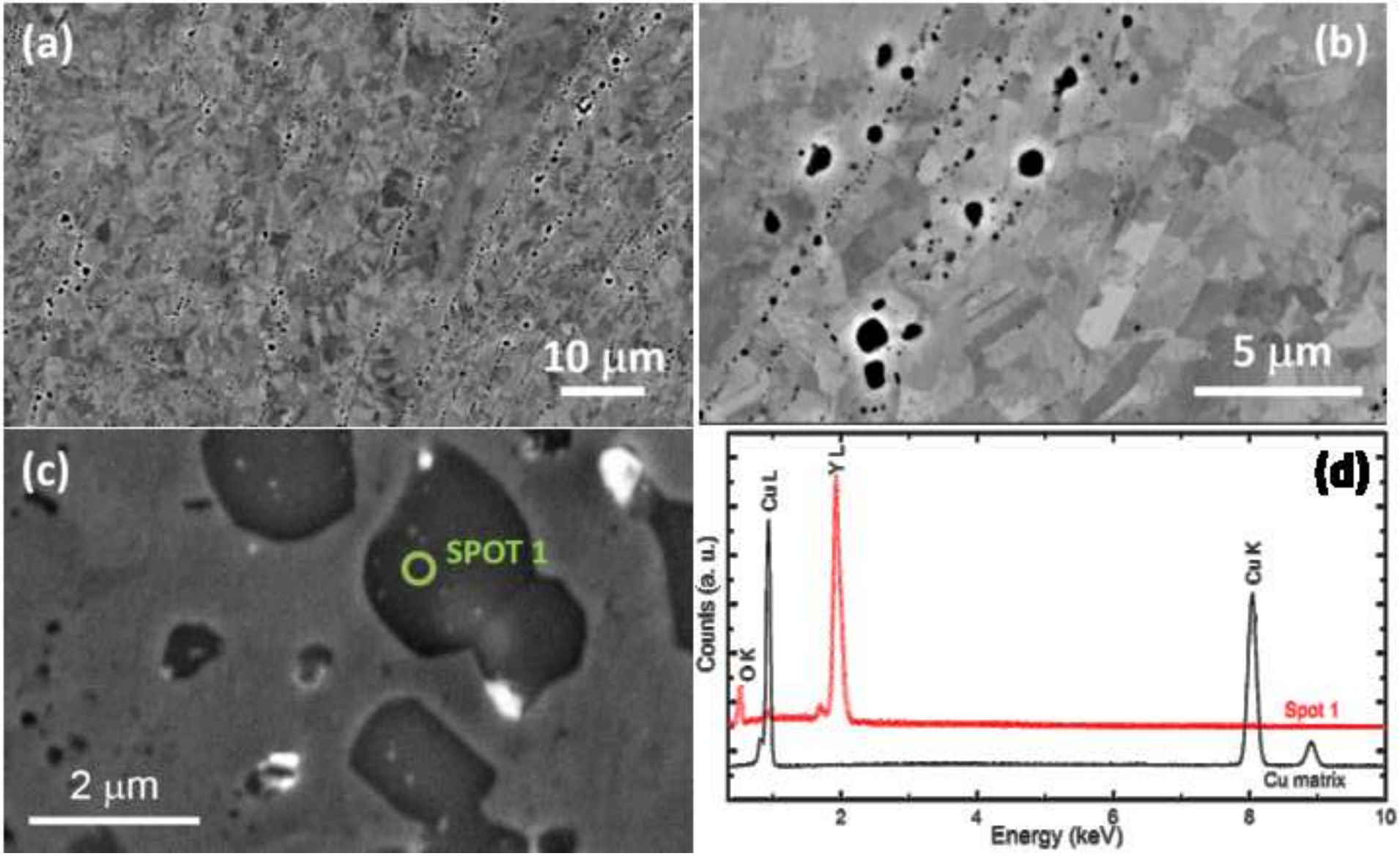

Figure9
Click here to download high resolution image

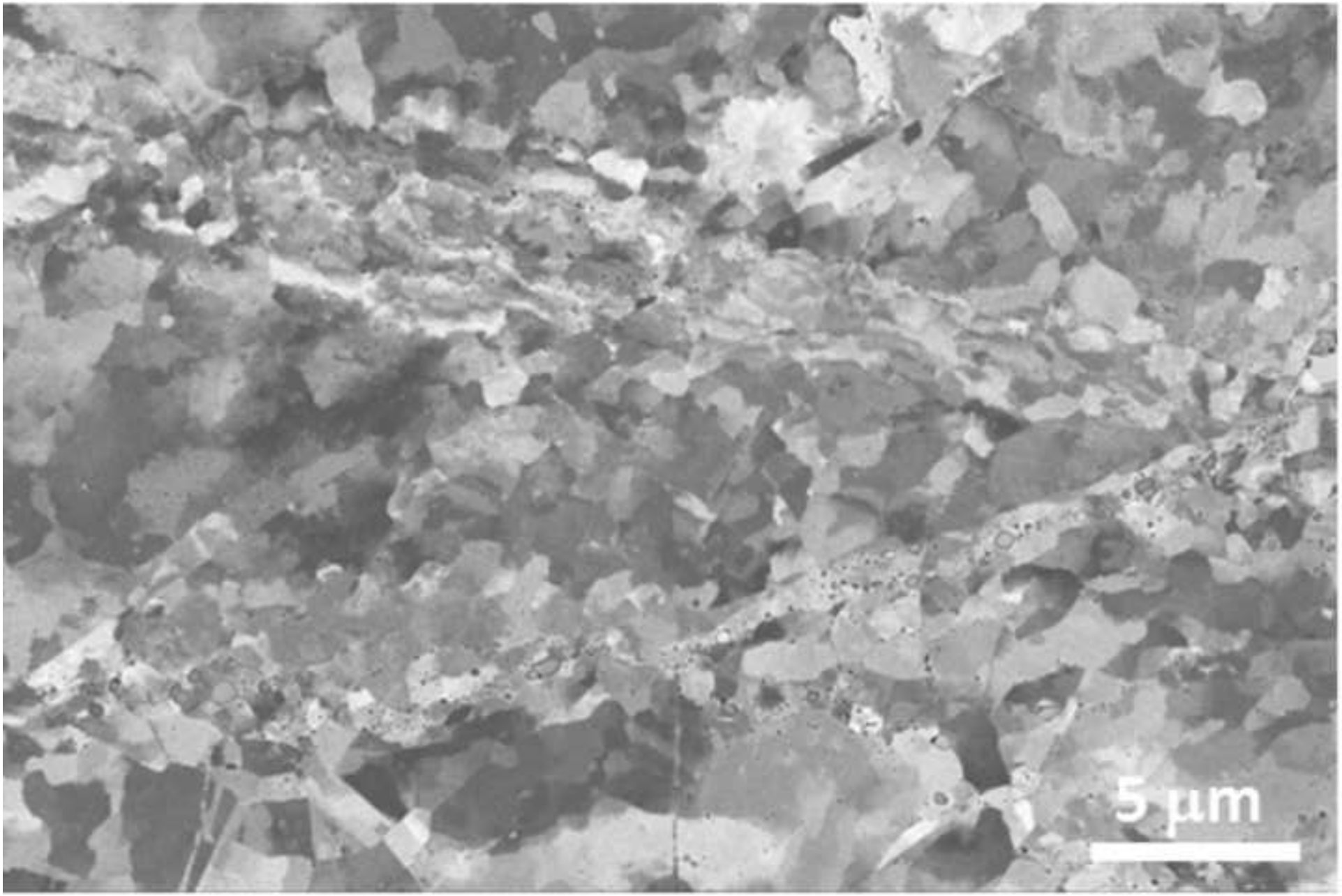

Figure10
Click here to download high resolution image

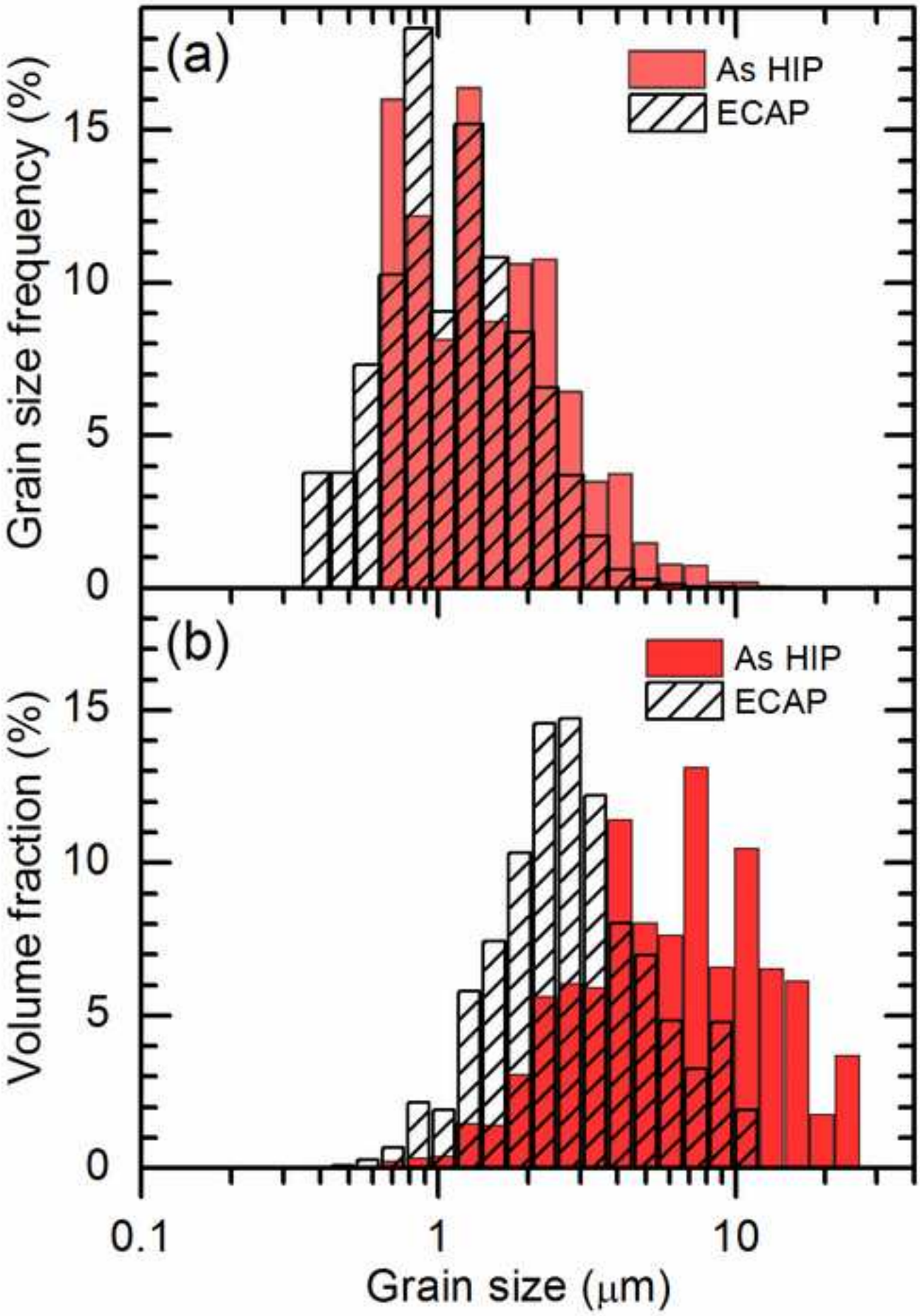

Figure11
Click here to download high resolution image

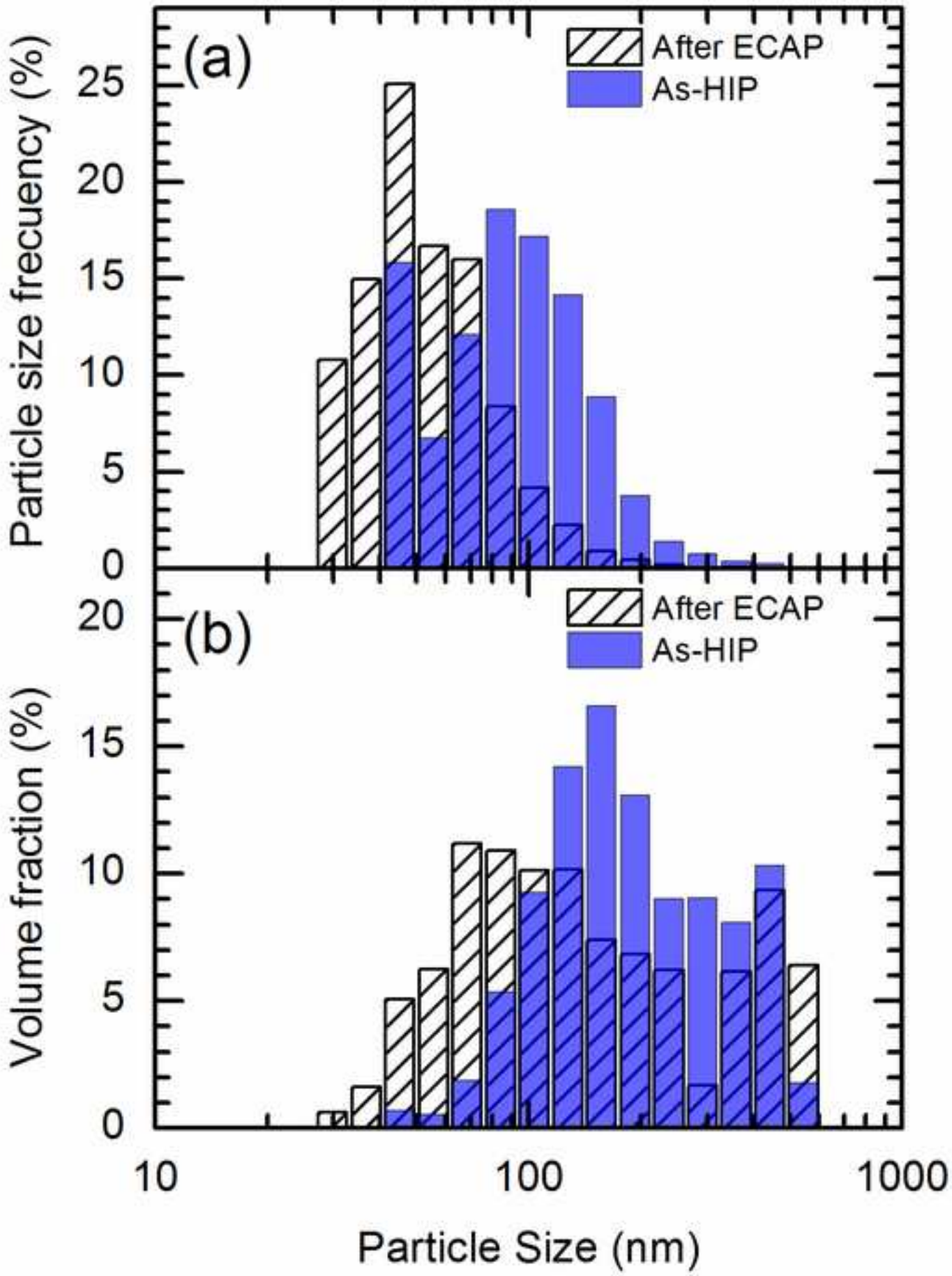

Figure12
Click here to download high resolution image

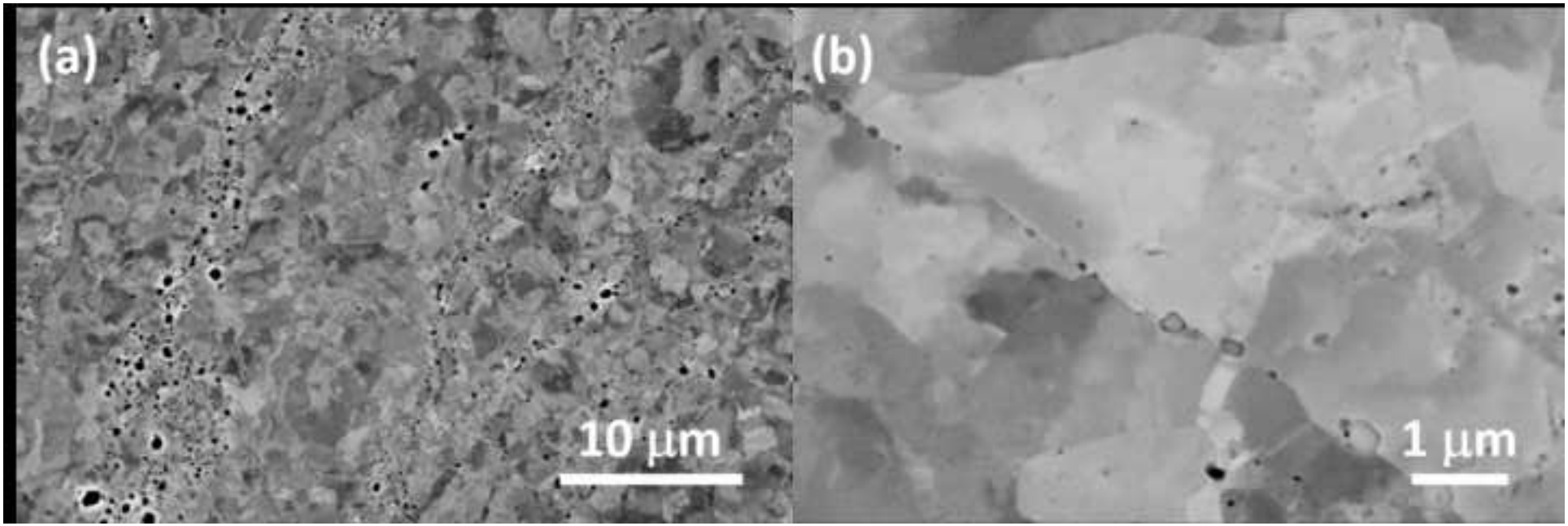

Figure13
Click here to download high resolution image

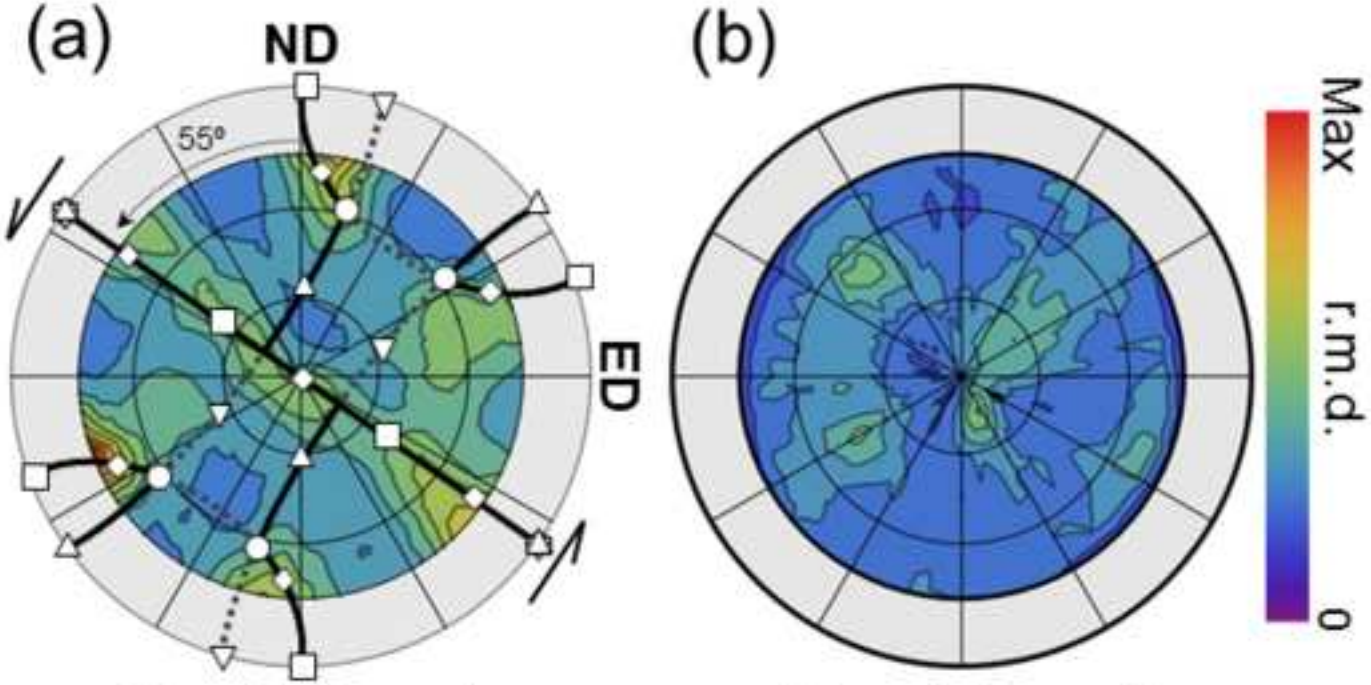

Main ideal orientations	
C – □	{0 0 1}⟨1 1 0⟩
A_1 – △	{1 1 1}[$\bar{1}$ $\bar{1}$ 2]
A_2 – ▽	(1 1 1) [1 1 $\bar{2}$]
A/$\bar{A}$ – ○	(1 $\bar{1}$ 1) [1 1 0] ($\bar{1}$ 1 $\bar{1}$) [$\bar{1}$ $\bar{1}$ 0]
B/$\bar{B}$ – ◊	(1 $\bar{1}$ 2)[1 1 0] ($\bar{1}$ 1 $\bar{2}$) [$\bar{1}$ $\bar{1}$ 0]

Figure14
Click here to download high resolution image

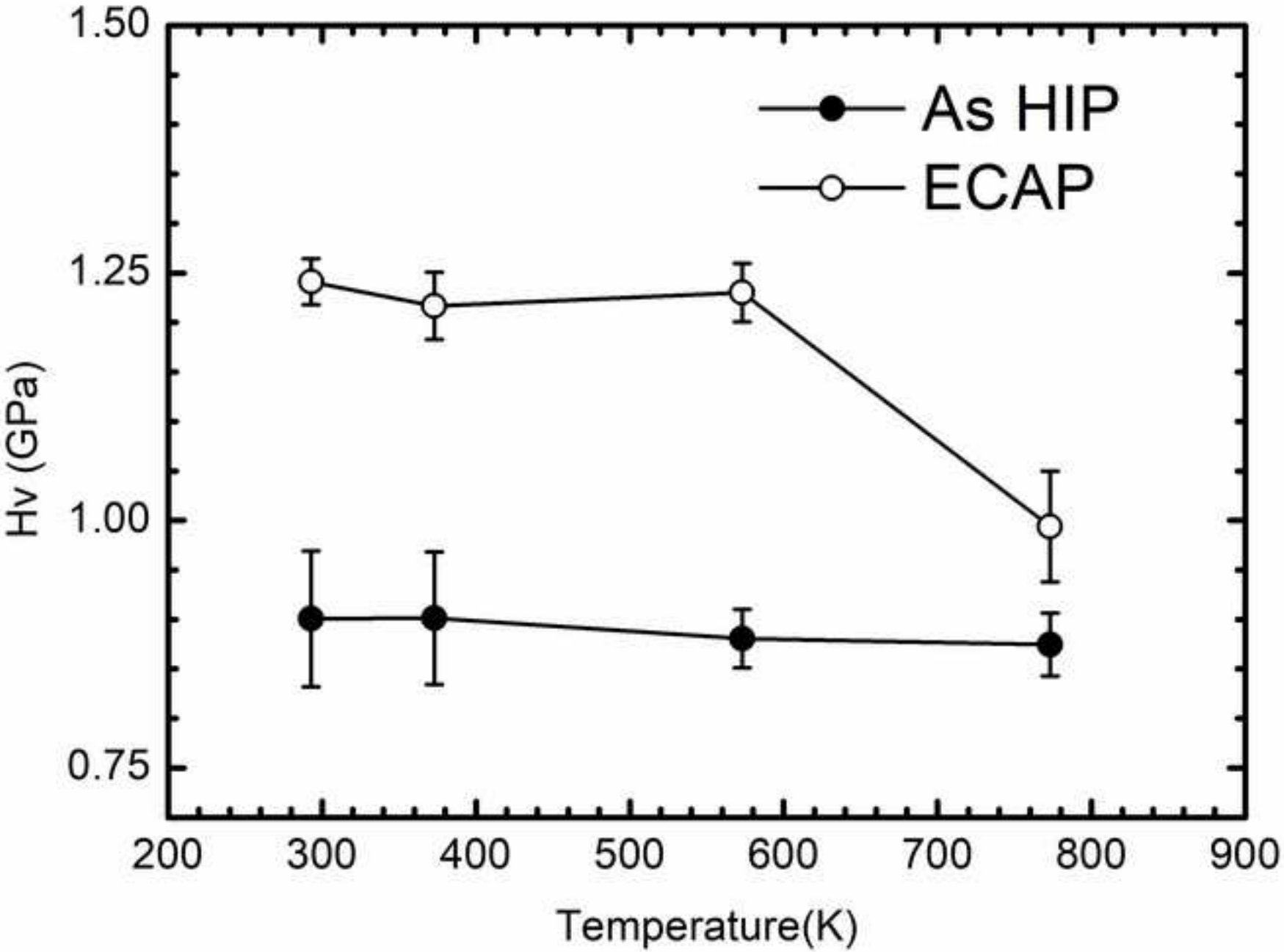

Figure15
Click here to download high resolution image

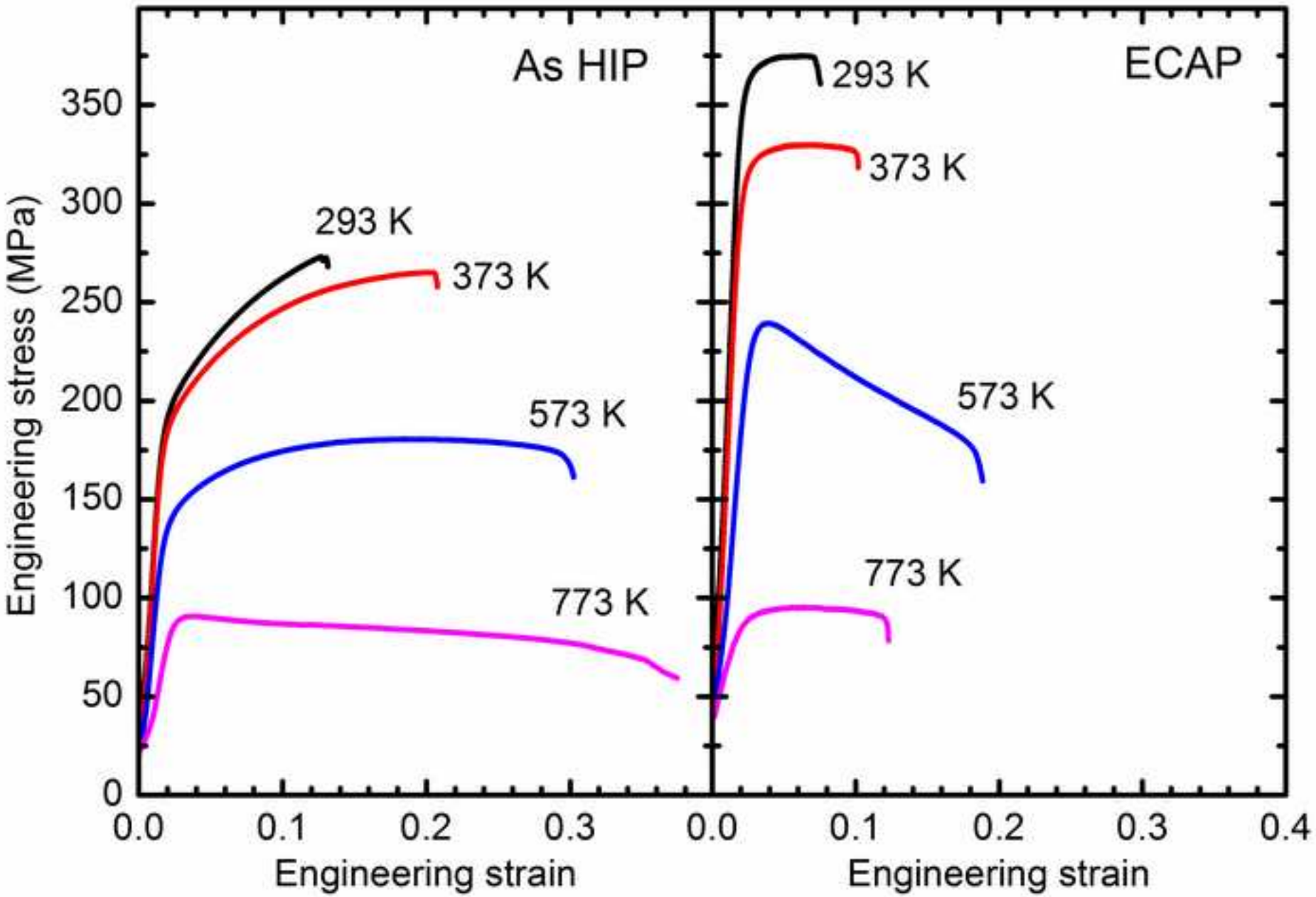

Figure16
Click here to download high resolution image

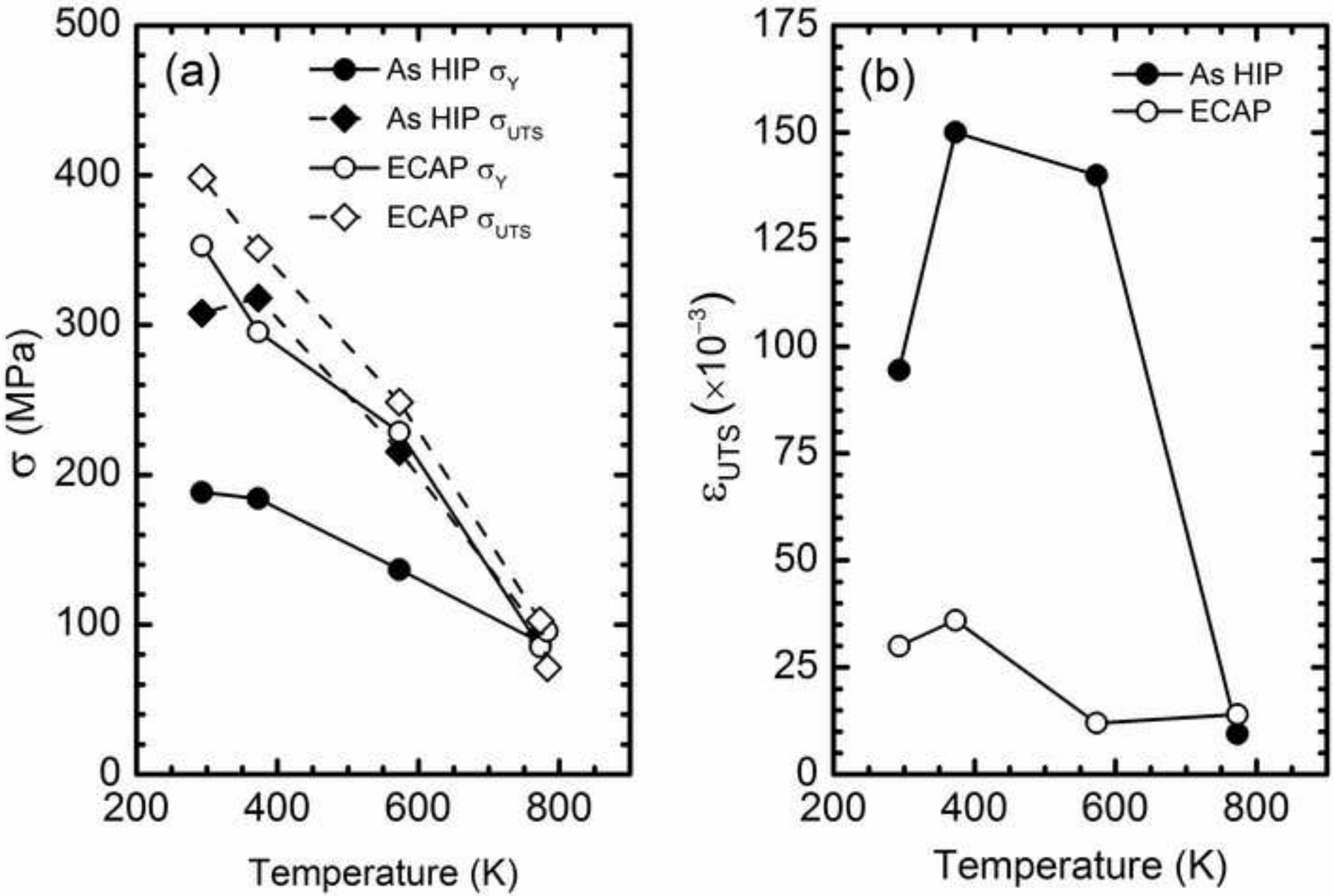

Figure17
Click here to download high resolution image

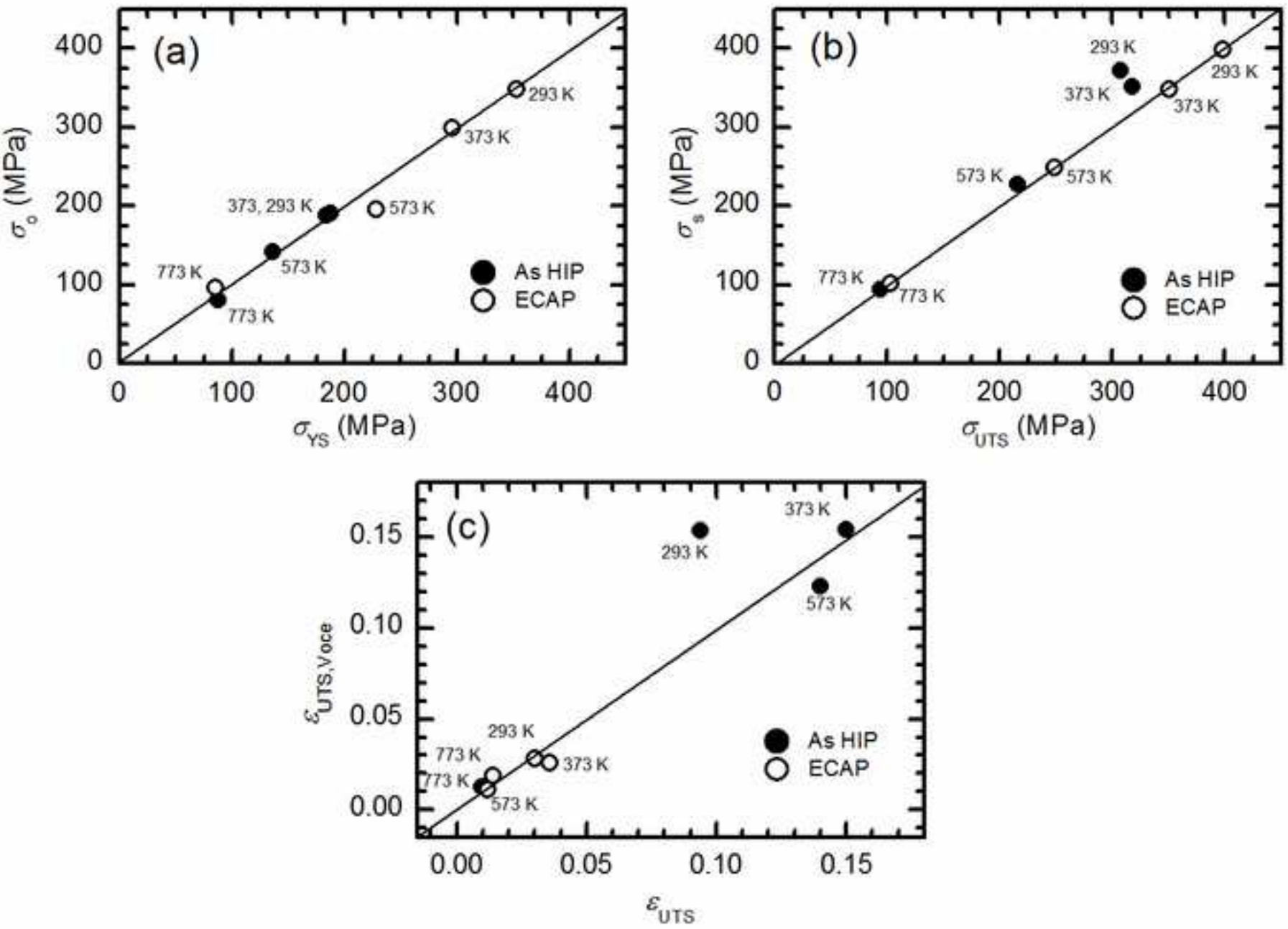

Figure18
Click here to download high resolution image

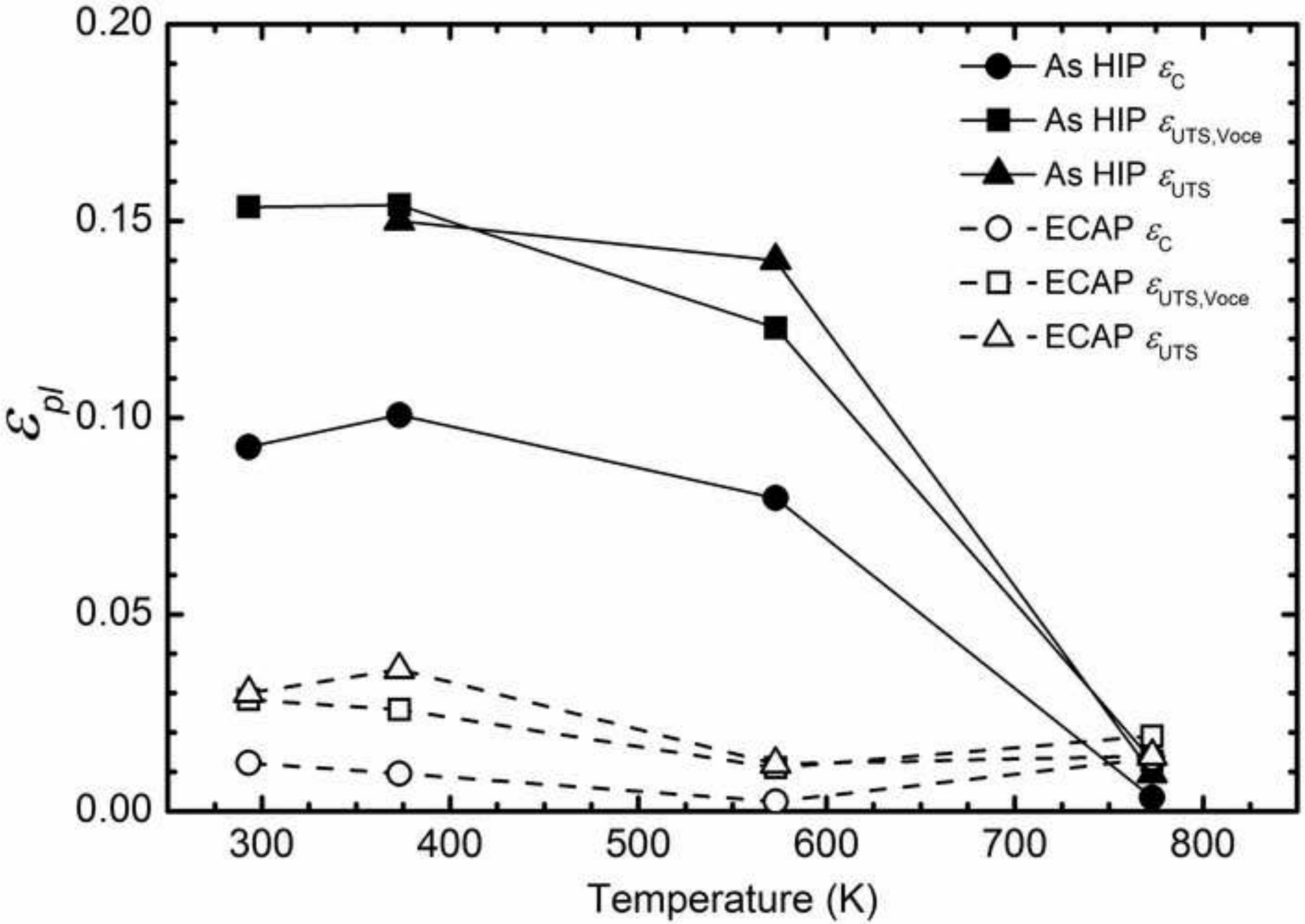

Figure19
Click here to download high resolution image

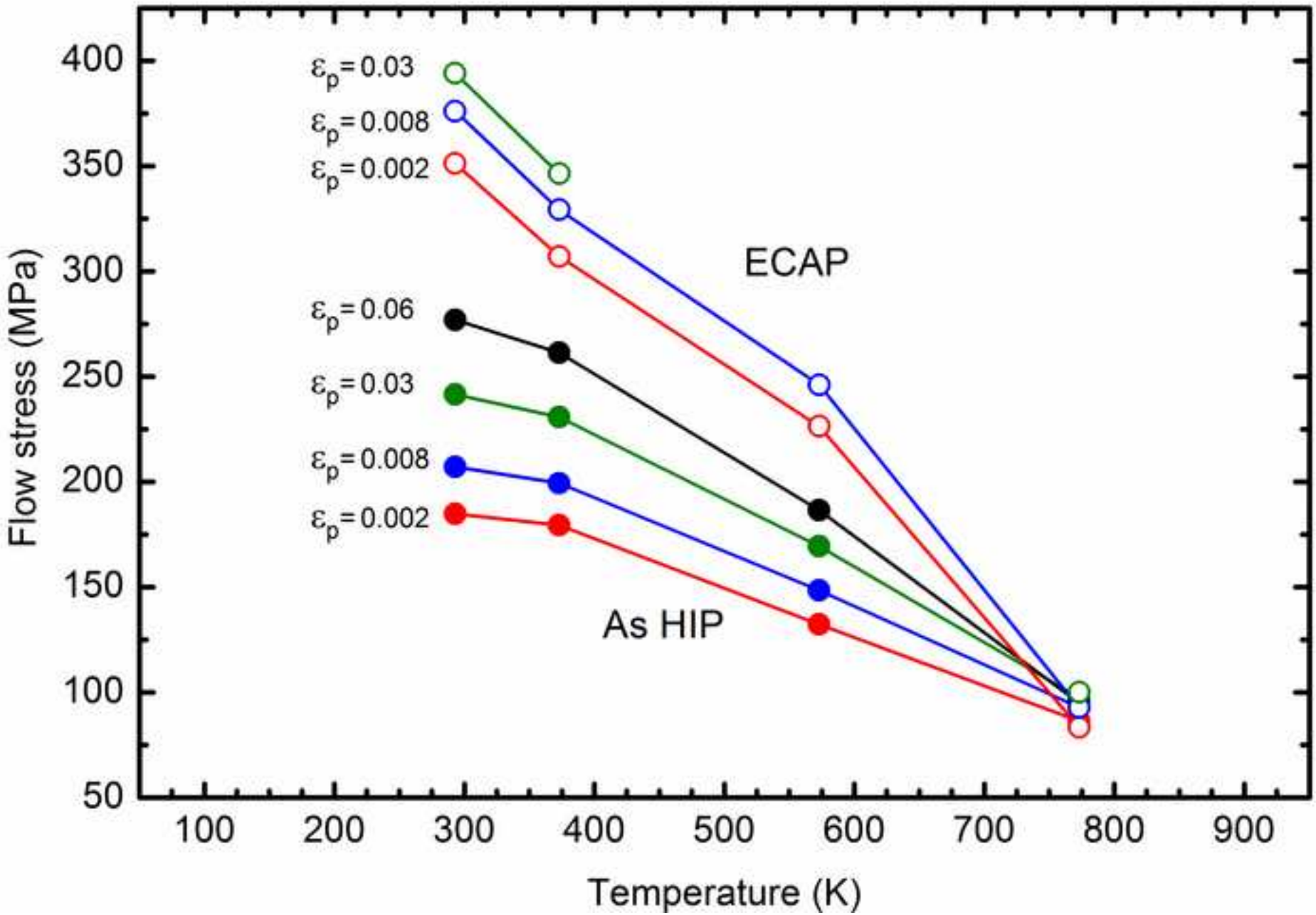

Figure20
Click here to download high resolution image

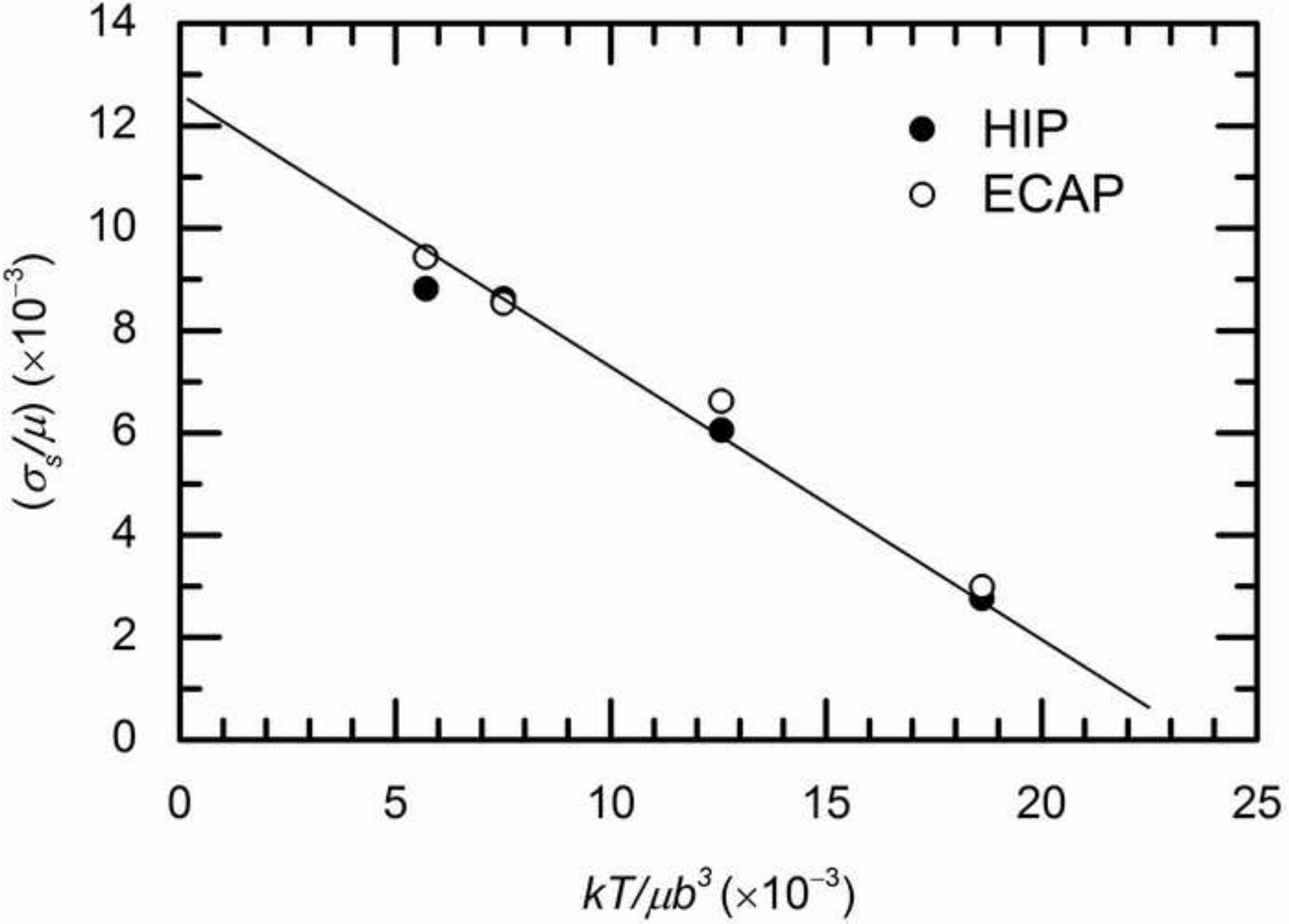

Figure21
Click here to download high resolution image